Identification of Physiological Response Functions to Correct for Fluctuations in Resting-State fMRI related to Heart Rate and Respiration

Michalis Kassinopoulos[1], Georgios D. Mitsis[2]

[1]Graduate Program in Biological and Biomedical Engineering, McGill University, Montreal, QC, Canada
[2]Department of Bioengineering, McGill University, Montreal, QC, Canada

Abstract

Functional magnetic resonance imaging (fMRI) is widely viewed as the gold standard for studying brain function due to its high spatial resolution and non-invasive nature. However, it is well established that changes in breathing patterns and heart rate influence strongly the BOLD fMRI signal and this, in turn, can have considerable effects on fMRI studies, particularly resting-state studies. The effects of physiological processes are often quantified by using convolutional models along with simultaneously recorded physiological data. In this context, physiological response function (PRF) curves (cardiac and respiratory response functions), which are convolved with the corresponding physiological fluctuations, are commonly employed. Initially, these PRF curves were assumed to be identical across subjects, but more recently, the use of subject-specific PRF curves has been suggested (derived by e.g. using the global fMRI signal). In the present study, we propose a novel framework for the robust estimation of PRF curves and use this framework to rigorously examine the implications of using population-, subject-, session- and scan-specific PRF curves. The proposed framework was tested on resting-state fMRI and physiological data from the Human Connectome Project. Our results suggest that PRF curves vary significantly across subjects and, to a lesser extent, across sessions from the same subject. These differences can be partly attributed to physiological variables such as the mean and variance of the heart rate during the scan. The proposed method can be used to obtain robust scan-specific PRF curves from data records with duration longer than 5 minutes, exhibiting significantly improved performance compared to previously defined canonical cardiac and respiration response functions. Besides removing physiological confounds from the BOLD signal, accurate modeling of subject- (or session-/scan-) specific PRF curves is of importance in studies that involve populations with altered vascular responses, such as aging subjects.

1. Introduction

Over the last few decades, advances in neuroimaging methods have significantly facilitated the study of brain function. One of the most popular methods for measuring brain activity is functional magnetic resonance imaging (fMRI), due to its high spatial resolution and non-invasive nature. fMRI, in principle, allows the mapping of brain function by measuring the hemodynamic response that accompanies neuronal activity in the brain. The onset of neuronal activity leads to physiological changes in the cerebrovascular system, including changes in cerebral blood flow (CBF), cerebral blood volume (CBV) per unit of brain tissue, as well as oxyhemoglobin and deoxyhemoglobin concentrations. The majority of fMRI studies is based on the blood-oxygenation-level-dependent (BOLD) contrast mechanism, which primarily corresponds to the concentration of deoxyhemoglobin, and, thus, reflects a complex interplay of the aforementioned physiological processes (Ogawa and Lee, 1990).

Intriguingly, low-frequency (< 0.15 Hz) fluctuations of the BOLD fMRI signal in the resting brain have consistently revealed significant correlations between distinct brain regions giving rise to a number of functional networks, named resting-state networks (RSNs) (Biswal et al., 1995; Smith et al., 2009). Furthermore, several studies have reported alterations of RSNs in a range of cerebrovascular and mental disorders, demonstrating their potential use as biomarkers (Demirtaş et al., 2016; Leonardi et al., 2013; Sheline et al., 2010; Woodward and Cascio, 2015). Therefore, while fMRI studies were initially focused on studying the function of individual brain regions in response to specific tasks, during the last two decades or so there has been a shift towards understanding the correlation between distinct brain regions during rest, referred to as resting-state functional connectivity (rs-FC; van den Heuvel and Hulshoff Pol, 2010).

However, the interpretation of rs-FC studies is often questioned, partly because of the challenge of disentangling the neuronal component of the BOLD signal, which is typically of interest, from measurement and physiological confounds (Bright and Murphy, 2015; Murphy et al., 2009). These confounds may be related to scanner hardware drifts and instabilities, head motion as well as spontaneous physiological fluctuations, including respiration and cardiac activity, as well as arterial CO2 (Caballero-Gaudes and Reynolds, 2017; Liang et al., 2015; Murphy et al., 2013; Wise et al., 2004). For instance, fluctuations in the BOLD signal arise from cardiac pulsation, which pushes the brainstem into the surrounding brain tissue, causing deformation and cerebrospinal fluid movement (Dagli et al., 1999) while respiration-induced fluctuations result partly from respiration-related bulk movement of the head (Hu et al., 1995). Also, variations in the rate or depth of respiration have an impact on the arterial tension of CO_2, which is a potent vasodilator and can therefore induce changes in CBF (Birn et al., 2006; Wise et al., 2004). In turn, global CBF changes cause low-frequency (~0.1 Hz) fluctuations in the BOLD signal, which may be misinterpreted as neuronal activity (Birn et al., 2008a, 2006). In addition, it has been shown that fluctuations in the BOLD signal are caused by spontaneous fluctuations in heart rate (Napadow et al., 2008; Shmueli et al., 2007). These physiological-related fluctuations can have considerable impact on the resulting rs-FC patterns, including dynamic rs-FC patterns, as they tend to inflate the correlation between areas affected by physiological noise (Birn et al., 2008a; Nikolaou et al., 2016). Therefore, several physiological noise correction techniques have been developed to remove the effects of physiological factors from fMRI data.

One of the most widely used methods for fMRI physiological noise correction is RETROICOR, proposed by Glover et al. (2000). According to this method, the pulsatility of blood flow and respiration-related motion are considered to distort the BOLD signal inducing an artifact that is time-locked to the cardiac and respiratory phases. Therefore, the associated physiological regressors are estimated as a linear combination of sinusoidal signals coinciding with the cardiac and respiratory cycles using concurrent cardiac and respiratory measurements and subsequently regressed out. RETROICOR can effectively remove the high-frequency cardiac (~1 Hz) and respiratory (~0.3 Hz) artifacts despite the aliasing that takes place in a typical fMRI acquisition with a relatively low sampling rate (e.g. TR=3 s; Jones et al., 2008).

Cardiac and respiratory recordings can be also used for reducing low-frequency BOLD fluctuations associated with changes in heart rate and breathing patterns using physiological response function (PRF) models, such as the ones proposed by Chang et al. (2009) and Birn et al. (2006, 2008b). In the first model, heart rate (HR) values, extracted from cardiac measurements, are convolved with the so-called cardiac response function (CRF). According to the second model, respiration volume per time (RVT), which is a measure proportional to the breathing rate (BR) and depth at each

time point, is initially estimated based on measurements from a pneumatic belt. Subsequently, RVT is convolved with the respiration response function (RRF) to estimate BOLD fluctuations due to changes in the breathing pattern. Both models are implemented in major fMRI preprocessing toolboxes such as the physiological noise modelling (PNM) toolbox of FSL (Jenkinson et al., 2012) and the PhysIO SPM toolbox (Kasper et al., 2017). Nevertheless, their use has been somewhat limited, partly due to that they do not account for between-subject PRF variability. In this context, Falahpour et al. (2013) proposed an alternate approach for constructing subject-specific PRF curves based on the global signal (GS), which is defined as the mean BOLD signal across all voxels in the brain, from each scan. Physiological regressors constructed in this way can account for a considerably larger fraction of variance in fMRI timeseries compared to the standard PRF curves. However, when individual PRF curves were used in a cross-validation analysis, the results suggested that the improvement in the explained variance may be due to overfitting (Falahpour et al., 2013).

Several data-driven approaches have been also proposed for preprocessing BOLD fMRI data. For example, in global signal regression (GSR), the GS is subtracted from the data through linear regression, implicitly assuming that processes that globally affect the fMRI BOLD signal are mostly uncorrelated to neural activity (Fox et al., 2005; Greicius et al., 2003; Qing et al., 2015). However, the validity of GSR is still under debate, as there is some evidence that the GS has a neuronal component as well (Liu et al., 2017; Murphy and Fox, 2017). Furthermore, the use of independent component analysis (ICA) or principal component analysis (PCA) to identify physiological or "noisy" components (based on their temporal, spatial and spectral features) and subsequently remove them before reconstructing the "noise-free" fMRI data, has been proposed (Churchill and Strother, 2013; Kay et al., 2013; Pruim et al., 2015a; Salimi-Khorshidi et al., 2014). For example, FIX ("FMRIB's ICA-based X-noisefier") implements a semi-automatic procedure for denoising fMRI via classification of ICA components. Due to its performance with respect to automatic and manual classification of "noisy" components, FIX has been used in the default resting-state fMRI preprocessing pipeline for generating HCP connectomes (Salimi-Khorshidi et al., 2014). However, recent studies have demonstrated that global fluctuations captured in the GS are still prominent after FIX-denoising (Burgess et al., 2016; Power et al., 2017). Additional studies have established a strong association of the GS with slow-frequency fluctuations of respiration and heart rate (Chang and Glover, 2009a; Falahpour et al., 2013). Overall, these studies suggest that FIX, and in general PCA/ICA-based noise correction techniques, may not sufficiently correct for these sources of noise.

In this context, we propose a novel methodological framework for extracting subject- and scan-specific PRF curves using the GS. We propose a double gamma structure for the PRF curves and a combination of optimization techniques (genetic algorithms and interior-point optimization) for parameter estimation. In contrast to previous approaches (Birn et al., 2008b; Chang et al., 2009; Falahpour et al., 2013), the convolution of physiological variables (HR, breathing pattern) with the PRF curves is done in a pseudo-continuous time-domain at a 10 Hz sampling frequency to avoid smoothing out the effect of high-frequency physiological fluctuations of HR. In addition to between-subject variability, we rigorously investigate the between-session variability of the PRF curves, as well as their variability across voxels in the brain. To this end, as well as to evaluate the performance of the proposed methodology, we use resting-state fMRI data from the Human Connectome Project (HCP; Van Essen et al., 2013) collected during 4 different scanning sessions on 2 different days. The noise correction techniques discussed here are also of importance for task-based studies, such as those involving motor and pain protocols, as fluctuations in cardiac activity and breathing patterns may be time-locked to the task, and, hence, bias the results (Glasser et al., 2018).

2. Methodology

2.1 Human Connectome Project (HCP) Dataset

We used resting-state scans from the HCP S1200 release (Glasser et al., 2016; Van Essen et al., 2013). The HCP dataset includes, among others, resting-state (eyes-open and fixation on a cross-hair) data from healthy young (age range: 22-35 years) individuals acquired on two different days. On each day, two 15-minute scans were collected. We refer to the two scans collected on days 1 and 2 as R1a/R1b and R2a/R2b respectively. fMRI acquisition was performed with a multiband factor of 8, spatial resolution of 2 mm isotropic voxels, and a TR of 0.72 s (Glasser et al., 2013).

The minimal preprocessing pipeline for the resting-state HCP dataset is described in (Glasser et al., 2013). In brief, the pipeline includes gradient-nonlinearity-induced distortion correction, motion correction, EPI image distortion correction, non-linear registration to MNI space and mild high-pass (2000 s) temporal filtering. The motion parameters are included in the database for further correction of motion artifacts. The HCP has adopted FIX for removing structured temporal noise related to motion, non-neuronal physiology, scanner artefacts and other nuisance sources (Salimi-Khorshidi et al., 2014). FIX-denoised data are available in the HCP database as well.

In the present work, we examined minimally-preprocessed and FIX-denoised data from 41 subjects (Supplementary Table 1), which included good quality physiological signals (cardiac and respiratory waveforms) in all four scans, as assessed by visual inspection. The cardiac and respiratory signals were collected with a photoplethysmograph and respiratory belt respectively.

2.2 Preprocessing

Unless stated otherwise, the preprocessing and analysis described below were performed in Matlab (R2017b; Mathworks, Natick MA).

2.2.1 Preprocessing of physiological recordings

The cardiac signal (i.e. photoplethysmogram) was initially band-pass filtered with a 2nd order Butterworth filter between 0.3 and 10 Hz. The minimum peak distance specified for peak detection varied between 0.5 and 0.9 seconds depending on the subject's average HR. The HR signal was computed in beats-per-minute (bpm) by multiplying the inverse of the time differences between pairs of adjacent peaks with 60, and evenly resampled at 10 Hz.

In the case of scans with abrupt changes in HR, if these changes were found by visual inspection to be due to noisy cardiac signal, then the HR signal was corrected for outliers using Matlab. Specifically, outliers in the HR signal were defined as the time points that deviated more than (approximately) 7 median absolute deviations (MAD) from the moving median value within a time window of 30 seconds. The MAD threshold varied across scans and was chosen empirically based on the extent of noise in the cardiac signal of each scan and the extracted HR signal. Outliers were replaced using linear interpolation (for examples of HR signals with abrupt changes and how they were treated, please see Supplementary Figs. 1 and 2).

The respiratory signal was detrended linearly and corrected for outliers using the moving median method described earlier. The duration of the moving time window and the MAD threshold were chosen separately for each scan based on visual inspection. Subsequently, the respiratory signal was low-pass filtered at 5 Hz with a 2nd order Butterworth filter and z-scored. The peak detection, used later for the extraction of RVT, was done with a minimum peak distance of 2 s and minimum peak height of 0.2.

2.2.2 *Preprocessing of fMRI data*

The effect of HR and respiratory variations on the fMRI BOLD signal is considered to last about half a minute (Chang et al., 2009). Therefore, the first 40 image volumes were disregarded, while the corresponding physiological data were retained. The fMRI timeseries were first spatially smoothed with a Gaussian filter of 3 mm full width at half maximum (FWHM) and then linearly detrended. Subsequently, the following nuisance variables were regressed out through linear regression: the demeaned and linearly detrended motion parameters and their derivatives, and 3rd order RETROICOR regressors for the cardiac and respiratory artifacts (Glover et al., 2000) using the physiological recordings at the original sampling rate of 400 Hz.

2.3 Physiological response functions

We employed linear dynamic models for extracting physiological regressors that were subsequently included in the general linear model as regressors to model the effect of the corresponding physiological variable on the BOLD signal. The physiological regressors were obtained as the convolution between the physiological variables and the corresponding PRF.

2.3.1 *Standard cardiac response function (CRF_{stand}; Chang et al. 2009)*

In the present study, the model proposed in Chang et al. (2009) was considered as the standard method for removing the effect of HR fluctuations. According to this method, the HR signal is smoothed with a 6 s moving average filter before being convolved with the standard CRF (CRF_{stand}) defined as:

$$CRF_{stand}(t) = 0.6t^{2.6}e^{-t/1.6} - 16\frac{1}{\sqrt{2\pi(9)}}e^{-\frac{1}{2}\frac{(t-12)^2}{9}}, \qquad [1.]$$

to construct the physiological regressor X_{HR} related to HR fluctuations. Finally, X_{HR} was downsampled to the fMRI sampling rate.

2.3.2 *Standard respiration response function (RRF_{stand}; Birn et al. 2006, 2008)*

We used the method described in (Birn et al., 2008b) as the standard method for removing the effect of changes in the breathing pattern. Briefly, the maximum and minimum peaks of each breath were initially identified on the respiratory signal and linearly interpolated at 10 Hz. Subsequently, the breathing depth was defined as the difference between the interpolated time-series of maximum and minimum peaks. The BR was calculated as the time difference between successive maximum peaks, expressed in breaths per minute (bpm; note the acronym bpm is used for both HR and BR and the distinction between them is based on the context of the sentence), and interpolated at 10 Hz. Subsequently, the respiration volume per time (RVT) was calculated as the product between breathing depth and rate. Finally, the RVT time-series were convolved with the standard RRF (RRF_{stand}) defined as:

$$RRF_{stand}(t) = 0.6t^{2.1}e^{-t/1.6} - 0.0023t^{3.54}e^{-t/4.25} \qquad [2.]$$

which yielded the physiological regressor X_{RVT} related to changes in the breathing pattern. Finally, X_{RVT} was downsampled to the fMRI sampling rate.

2.3.3 *Proposed physiological response functions (PRF)*

Here, we used the instantaneous HR without any smoothing, whereas the respiratory signal was first filtered with a moving average window of 1.5 s and the square of its derivative was subsequently calculated. The respiratory signal was smoothed before calculating the derivative to avoid large, physiologically implausible spikes in the extracted regressor. The signal extracted after this process, termed respiratory flow (RF), reflects the absolute flow of the inhalation and exhalation of the subject at each time point. While RF carries similar information with RVT, it is expected to be more

robust as it does not depend on accurate peak detection. To reduce the time of subsequent analysis, RF was downsampled from 400 Hz to 10 Hz. Therefore, the corresponding physiological regressors were defined as follows:

$$X_{HR}(t) = HR * CRF, \text{ and} \quad [3.]$$

$$X_{RF}(t) = RF * RRF \quad [4.]$$

where CRF and RRF are the proposed cardiac and respiration response functions, respectively. The basic structure of the two proposed PRF curves was selected as the double gamma function that is also used for RRF_{stand} and the canonical hemodynamic response function (HRF) in the SPM software package (http://www.fil.ion.ucl.ac.uk/spm/). The gamma function is defined as:

$$\Gamma(\tau, \delta, t) = a(\tau, \delta) \cdot t^{\frac{\sqrt{\tau}}{\delta}} \cdot e^{-\frac{t}{\delta\sqrt{\tau}}}, \quad [5.]$$

The parameters τ and δ indicate the (approximate) time of peak and dispersion of the function, and the parameter α is a scaling factor which normalizes the peak value of the gamma function to 1. The PRF curves are defined as follows:

$$\begin{aligned} CRF(t) &= \beta_{1,c} \cdot \Gamma(\tau_{1,c}, \delta_{1,c}, t) + \beta_{2,c} \cdot \Gamma(\tau_{2,c}, \delta_{2,c}, t)\,, \\ RRF(t) &= \beta_{1,r} \cdot \Gamma(\tau_{1,r}, \delta_{1,r}, t) + \beta_{2,r} \cdot \Gamma(\tau_{2,r}, \delta_{2,r}, t)\,. \end{aligned} \quad [6.]$$

Below, we collectively refer to the eight parameters of the gamma functions ($\tau_{1,c}, \delta_{1,c}, \tau_{2,c}, \delta_{2,c}, \tau_{1,r}, \delta_{1,r}, \tau_{2,r}, \delta_{2,r}$) and the four scaling parameters ($\beta_{1,c}, \beta_{2,c}, \beta_{1,r}, \beta_{2,r}$) as $\boldsymbol{G}$ and $\boldsymbol{B}$ respectively. Note that, since the PRF curves have arbitrary units, they can be expressed as follows:

$$\begin{aligned} CRF(t) &= \beta_c\left[\Gamma(\tau_{1,c}, \delta_{1,c}, t) + R_c \cdot \Gamma(\tau_{2,c}, \delta_{2,c}, t)\right]\,, \\ RRF(t) &= \beta_r\left[\Gamma(\tau_{1,r}, \delta_{1,r}, t) + R_r \cdot \Gamma(\tau_{2,r}, \delta_{2,r}, t)\right]\,. \end{aligned} \quad [7.]$$

where the parameters R_c and R_r correspond to the ratios $\beta_{2,c}/\beta_{1,c}$ and $\beta_{2,r}/\beta_{1,r}$, respectively, and the two scaling parameters β_c and β_r reflect the amount of variance explained by the corresponding physiological variables on the BOLD signal under investigation. Finally, the extracted physiological regressors were downsampled to the fMRI acquisition rate.

2.4 Comparison of different physiological models

Previous studies have suggested that subject-specific PRF curves may be more appropriate for constructing physiological regressors (Birn et al., 2008b; Chang et al., 2009; Falahpour et al., 2013). Here, we rigorously examined this hypothesis by considering several different cases for estimating the PRF curve parameters and assessing the resulting performance. For each subject, we used four different 15-minute resting-state scans collected on two different sessions (days): R1a/R1b (day one) and R2a/R2b (day two). This allowed us to examine the variability of the PRF curves between subjects, as well as between scans and sessions of the same subject. Initially (Section 2.4.1), we considered three main models, particularly two variants of population-specific models and a scan-specific model to examine the variability in the shape of the PRF curves across scans for models with different degree of flexibility. Subsequently (Section 2.4.2), we assessed the performance of several variants of PRF models with respect to the explained variance to examine whether the use of subject-, session- or scan- specific PRF is justifiable. In both cases, the GS from each scan was used to define the PRF curves and assess model performance. To extend these results (Section 2.4.3), we compared the performance of a subset of the models considered in 2.4.2 as well as the performance of a voxel-specific model in individual voxels.

2.4.1 Variability in the shape of the PRF curves across scans

Here, we aimed to examine the variability in the shape of PRF curves across scans for models based on different degree of flexibility. In addition, we aimed to understand the relation of the variability in shape to physiological variables such

as the mean HR. To this end, we examined three variants of the proposed PRF curves, termed PRF_{ppl}, PRF_{ppl}^{sc} and PRF_{sc} that were used to explain fluctuations on the GS of each scan. The PRF_{ppl} population-specific model is based on Eq. 7 and is the least flexible model, as it assumes that $\boldsymbol{G}$ (i.e., $\tau_{1,c}, \delta_{1,c}, \tau_{2,c}, \delta_{2,c}, \tau_{1,r}, \delta_{1,r}, \tau_{2,r}, \delta_{2,r}$) and $\boldsymbol{R}$ (i.e., R_c, R_r) are the same for all subjects. In this model, only $\boldsymbol{B}$ (i.e., β_c, β_r), which determines the amount of variance explained by HR and breathing pattern on the GS for each scan, was allowed to vary across scans. The PRF_{ppl}^{sc} model is also a population-specific model that allows variability in the shape of the PRF curves between scans. Specifically, it is based on Eq. 6 and it assumes that $\boldsymbol{G}$ ($\tau_{1,c}, \delta_{1,c}, \tau_{2,c}, \delta_{2,c}, \tau_{1,r}, \delta_{1,r}, \tau_{2,r}, \delta_{2,r}$) is the same for all subjects while $\boldsymbol{B}$ (i.e., $\beta_{1,c}, \beta_{2,c}, \beta_{1,r}, \beta_{2,r}$) was allowed to vary across scans. However, in this case, $\boldsymbol{B}$ determines both the amount of variance explained by the physiological variables on the GS as well as the shape of the PRF curves. Finally, PRF_{sc} is a scan-specific model also based on Eq. 6, in which all the parameters were allowed to vary across scans. The PRF parameters were estimated with non-linear optimization techniques described in Section 2.4.1.1.

In the case of the scan-specific model PRF_{sc}, apart from comparing the curves with their standard counterparts and population-specific PRF_{ppl} curves, we also examined whether the physiological variables for each scan can explain the between-scan variability in the shape of the curves as well as the performance with respect to the explained variance on the GS. Specifically, we examined whether the mean and variance of HR and BR/RF were correlated with the time of positive and negative peaks for CRF_{sc} and RRF_{sc}, respectively. In addition, we examined whether the mean and variance of HR and BR/RF were correlated to the correlation coefficient values between the associated physiological regressors (Eqs. 3-4) and the GS. Overall, we examined the relationship of 18 pairs of variables consisting of 6 explanatory variables, the mean and variance of HR, BR and RF, and 6 dependent variables, the time of positive and negative peak of the CRF_{sc}/RRF_{sc} curves as well as the correlation coefficient between the associated physiological regressors and the GS. Pairs of variables related to both HR and breathing pattern (e.g. mean of HR and time of positive peak for RRF_{sc}) were not considered. Regarding statistical testing, we used an alpha level of .05 adjusted for multiple comparisons (N=18) with Bonferroni correction.

2.4.1.1 PRF parameter estimation

The parameters of the population-specific model PRF_{ppl} were set to those that maximized the value returned by the following algorithm and were estimated using numerical optimization techniques (for a pseudocode of the algorithm, please see Supplementary Table 2): 1. for a set of given parameters, the two PRF_{ppl} curves were constructed. Subsequently, for each scan, 2. the HR and RF signals (sampled at 10 Hz) were convolved with CRF_{ppl} and RRF_{ppl} respectively to extract the corresponding physiological regressors and then downsampled to match the fMRI acquisition rate. 3. linear regression analysis was performed, whereby the GS was the dependent variable and the two physiological regressors were the two explanatory variables. 4. the Pearson correlation coefficient between the GS and the model prediction was calculated and 5. after performing steps 1-4 for all scans, the correlation value was averaged across all scans and returned by the algorithm.

In the case of PRF_{ppl}^{sc}, steps 2 and 3 were implemented as follows: In step 2, the two gamma functions for each PRF_{ppl}^{sc} curve were convolved separately with HR and RF. As a result, in step 3, two physiological regressors related to HR and two regressors related to RF were included in the linear regression model as explanatory variables (for a pseudocode of the algorithms for the PRF_{ppl} and PRF_{ppl}^{sc} models, please see Supplementary Table 2). Finally, the procedure described above was followed for the estimation of the parameters in the scan-specific model PRF_{sc}, with the only difference being that step 5 was omitted, as the PRF_{sc} parameters were estimated separately for each scan.

To obtain the optimal parameter values for the PRF_{ppl} model, a genetic algorithm (GA) implemented in Matlab R2017b's Global Optimization Toolbox was initially applied. GAs are a family of popular heuristic optimization techniques that search the parameter space for the optimal solution of a problem in a manner inspired by Darwin's principle of natural selection (Holland, 1975). GAs have generally higher demands in CPU time compared to gradient-based algorithms, but they are capable of providing potentially global optimal solutions for complex functions (Patel and Padhiyar, 2015). The

parameters $\boldsymbol{\tau}$ $(\tau_{1,c}, \tau_{2,c}\ \tau_{1,r}, \tau_{2,r})$ and $\boldsymbol{\delta}$ $(\delta_{1,c}, \delta_{2,c}, \delta_{1,r}, \delta_{2,r})$ were bounded between 0-20 seconds and 0-3 seconds, respectively. A stopping criterion of 100 generations was set, as it was found to be adequate for convergence. The solution of the GA was subsequently used as the initial point for the interior-point gradient-based algorithm, also implemented in Matlab R2017b (Optimization Toolbox), with a stopping criterion of 100 maximum iterations, to refine the solution.

To accelerate the estimation procedure for the remaining models, the obtained PRF_{ppl} parameter values (or curves) were used as the initial point for all models and the interior-point algorithm was employed with a stopping criterion of 100 maximum iterations to refine the solution. Moreover, since the parameter estimation for the scan-specific models was performed using a smaller amount of data, making these models more prone to overfitting, the upper and lower boundaries for $\boldsymbol{\tau}$ and $\boldsymbol{\delta}$ were restricted to non-negative numbers (±3 sec compared to the population-specific PRF_{ppl} model parameter values).

2.4.2 Comparison of population-, subject-, session- and scan-specific PRF curves

This section aimed to assess the performance of 13 different models (Table 1) with respect to the explained variance using two-level cross-validation (CV) to examine whether PRF curves significantly vary between subjects as well as between sessions or scans within subject. For each model, the PRF parameters were estimated from one segment of data (training set at the first-level of CV; 3rd column of Table 1) and model performance was assessed in a separate segment of data (validation set at the first-level of CV; 4th column of Table 1) as described in sections 2.4.2.1 and 2.4.2.2, respectively.

2.4.2.1 PRF parameter estimation at the first-level of cross-validation

The PRF models listed in Table 1 are, to some extent, sorted by the least to the most flexible model. The first six models (PRF_{ppl} to $PRF_{sbj,sdd}$) are based on Eq. 7. In this case, $\boldsymbol{R}$ (R_c, R_r), along with $\boldsymbol{G}$ $(\tau_{1,c}, \delta_{1,c}, \tau_{2,c}, \delta_{2,c}, \tau_{1,r}, \delta_{1,r}, \tau_{2,r}, \delta_{2,r})$, define the shape of the PRF curves; they were assumed to be population-specific for PRF_{ppl} and subject-specific for models $PRF_{sbj,d}$ to $PRF_{sbj,sdd}$. In these models, $\boldsymbol{B}$ (β_c, β_r) reflects the amount of explained variance of each physiological variable on the GS. The last 7 models (PRF_{ppl}^{sc} to PRF_{sc}) are based on Eq. 6. The PRF_{ppl}^{sc} model assumes that $\boldsymbol{G}$ is population-specific, the models $PRF_{sbj,d}^{sc}$ to $PRF_{sbj,sdd}^{sc}$ assume that $\boldsymbol{G}$ is subject-specific, while the PRF_{sc} model assumes that it is scan-specific. In the last seven models $\boldsymbol{B}$ $(\beta_{1,c}, \beta_{2,c}, \beta_{1,r}, \beta_{2,r})$ defines the amount of explained variance of the physiological variables on the GS as well as the shape of the PRF curves. As described in Section 2.4.1, in all 13 models, the interior-point gradient-based algorithm was applied after being initialized with the parameter values obtained from the population-specific model PRF_{ppl} (for a pseudocode of the algorithm used to estimate the PRF parameters in all 13 models, please see Supplementary Table 2).

The following notation was adopted: the subscript in the six models PRF_{ppl} to $PRF_{sbj,sdd}$ (Table 1) indicates whether $\boldsymbol{G}$ and $\boldsymbol{R}$ were estimated from the entire *population* ('ppl') or a different scan of the same *subject* ('sbj'). The letters 'd' and 's' in the subscript indicate whether parameter estimation and model performance were implemented using data from one or more scans collected during a *different* or *same* scanning session. For example, $PRF_{sbj,dd}$ denotes that $\boldsymbol{G}$ and $\boldsymbol{R}$ were estimated using data from two scans collected during one session (e.g. R1a/R1b) and model performance was assessed using data from a scan collected during a different session (e.g. R2a) from the same subject. Similarly, the subscript in the seven models PRF_{ppl}^{sc} to $PRF_{sbj,sdd}^{sc}$ indicates whether $\boldsymbol{G}$ was estimated from the entire *population* ('ppl'), a different scan of the same *subject* ('sbj') or the same *scan* ('sc'). In addition, the superscript 'sc' in the six models PRF_{ppl}^{sc} to $PRF_{sbj,sdd}^{sc}$ (Table 1) indicates that, even though $\boldsymbol{G}$ may be population- or subject-specific, the ultimate PRF shape is different for each *scan*. This is due to that $\boldsymbol{B}$, which was estimated for each scan separately, in the six models PRF_{ppl}^{sc} to $PRF_{sbj,sdd}^{sc}$ it consists of four parameters (i.e., $\beta_{1,c}, \beta_{2,c}, \beta_{1,r}, \beta_{2,r}$), in contrast to the first 6 models for which $\boldsymbol{B}$ consists of two parameters (i.e., β_c, β_r), allowing some flexibility in the shape of the PRF. Finally, the subscript 'sc'

Table 1. Assessment of the performance of population-, subject-, session- and scan- specific PRF models using two-level cross-validation (CV; $stand$: standard, ppl: population, sbj: subject, sc: scan, d: different, s: same)

Model:	**Estimated PRF parameters (non-linear optimization):**	**Obtained from (training set at the first-level of CV):**	**Model performance assessed on (validation set at the first-level of CV):**	**Estimated linear regression parameters (B):**
PRF_{stand}	---	Eqs. 1 and 2	any scan	β_c, β_r
PRF_{ppl}	$\tau_{1,c}, \delta_{1,c}, \tau_{2,c}, \delta_{2,c}, R_c,$ $\tau_{1,r}, \delta_{1,r}, \tau_{2,r}, \delta_{2,r}, R_r$	entire population - leave one out cross-validation (LOOCV; e.g. estimate parameters from set of subjects $\boldsymbol{S}^{\mid i} = \{S_1, S_2, .., S_{i-1}, S_{i+1}, S_{i+2}, .., S_{41}\}$ when the model performance is assessed for subject S_i)	any scan of subject S_i	same as PRF_{stand}
$PRF_{sbj,d}$	same as PRF_{ppl}	one scan; scan $R_{i,\{a,b\}}$ of subject S_x	scan $R_{j,\{a,b\}}$ from *different* session (day) of subject S_x where $i \neq j$	same as PRF_{stand}
$PRF_{sbj,dd}$	same as PRF_{ppl}	two scans of a session; scans $R_{i,a}$ & $R_{i,b}$ of subject S_x where $i = \{1,2\}$	scan $R_{j,\{a,b\}}$ from *different* session of subject S_x where $j = \{1,2\}$ and $i \neq j$	same as PRF_{stand}
$PRF_{sbj,s}$	same as PRF_{ppl}	one scan; scan $R_{i,j}$ of subject S_x where $i = \{1,2\}$ and $j = \{a, b\}$	scan $R_{i,k}$ from *same* session of subject S_x where $k = \{a, b\}$ and $j \neq k$	same as PRF_{stand}
$PRF_{sbj,sd}$	same as PRF_{ppl}	one scan of each session; scans $R_{i,j}$ & $R_{k,\{a,b\}}$ of subject S_x where $i = \{1,2\}$, $j = \{a, b\}$, $k = \{1,2\}$ and $i \neq k$	a different scan $R_{i,l}$ of subject S_x where $l = \{a, b\}$ and $j \neq l$	same as PRF_{stand}
$PRF_{sbj,sdd}$	same as PRF_{ppl}	three scans; scans $R_{i,j}$, $R_{k,a}$ and $R_{k,b}$ of subject S_x where $i = \{1,2\}$, $j = \{a, b\}$, $k = \{1,2\}$ and $i \neq k$	a different scan $R_{i,l}$ of subject S_x where $l = \{a, b\}$ and $j \neq l$	same as PRF_{stand}
PRF_{ppl}^{sc}	$\tau_{1,c}, \delta_{1,c}, \tau_{2,c}, \delta_{2,c},$ $\tau_{1,r}, \delta_{1,r}, \tau_{2,r}, \delta_{2,r}$	entire population - leave one out cross-validation (LOOCV; e.g. estimate parameters from set of subjects $\boldsymbol{S}^{\mid i} = \{S_1, S_2, .., S_{i-1}, S_{i+1}, S_{i+2}, .., S_{41}\}$ when the model performance is assessed for subject S_i)	any scan of subject S_i	$\beta_{1,c}, \beta_{2,c},$ $\beta_{1,r}, \beta_{2,r}$
$PRF_{sbj,d}^{sc}$	same as PRF_{ppl}^{sc}	one scan; scan $R_{i,\{a,b\}}$ of subject S_x where $i = \{1,2\}$	scan $R_{j,\{a,b\}}$ from *different* session of subject S_x where $i \neq j$	same as PRF_{pop}^{sc}
$PRF_{sbj,dd}^{sc}$	same as PRF_{ppl}^{sc}	two scans of a session; scans $R_{i,a}$ & $R_{i,b}$ of subject S_x where $i = \{1,2\}$	scan $R_{j,\{a,b\}}$ from *different* session of subject S_x where $i \neq j$	same as PRF_{pop}^{sc}
$PRF_{sbj,s}^{sc}$	same as PRF_{ppl}^{sc}	one scan; scan $R_{i,j}$ of subject S_x where $i = \{1,2\}$ and $j = \{a, b\}$	scan $R_{i,k}$ from *same* session of subject S_x where $k = \{a, b\}$ and $j \neq k$	same as PRF_{ppl}^{sc}
$PRF_{sbj,sd}^{sc}$	same as PRF_{ppl}^{sc}	one scan of each session; scans $R_{i,j}$ & $R_{k,\{a,b\}}$ of subject S_x where $i = \{1,2\}$, $j = \{a, b\}$ $k = \{1,2\}$ and $i \neq k$	a different scan $R_{i,l}$ of subject S_x where $l = \{a, b\}$ and $j \neq l$	same as PRF_{ppl}^{sc}
$PRF_{sbj,sdd}^{sc}$	same as PRF_{ppl}^{sc}	three scans; scans $R_{i,j}$, $R_{k,a}$ and $R_{k,b}$ of subject S_x where $i = \{1,2\}$, $j = \{a, b\}$, $k = \{1,2\}$ and $i \neq k$	a different scan $R_{i,l}$ of subject S_x where $l = \{a, b\}$ and $j \neq l$	same as PRF_{ppl}^{sc}
PRF_{sc}	same as PRF_{ppl}^{sc}	one scan; scan $R_{i,j}$ of subject S_x where $i = \{1,2\}$ and $j = \{a, b\}$	the same scan $R_{i,j}$ of subject S_x	same as PRF_{ppl}^{sc}

for the last model (PRF_{sc}) indicates that both $\boldsymbol{G}$ and $\boldsymbol{B}$ were estimated from data collected during the same scan; therefore, this was the most flexible model (for schematic examples of training and validation sets for each model, please see Supplementary Fig. 3).

To assess the performance of the population-specific models PRF_{ppl} and PRF_{ppl}^{sc}, a leave-one-out cross-validation (LOOCV) approach was implemented at the first-level, whereby the PRF curves were obtained using training data from 40 subjects and validated with data from the remaining subject. In the case of subject-specific models of the form $PRF_{sbj,x}^{x}$, we considered all possible scan combinations (instead of using only one of the scans as the validation data set) to examine the effect of session on the variability of PRF curves (e.g. $PRF_{sbj,d}$ vs $PRF_{sbj,s}$) as well as the dependence of the model performance on the amount of training data (e.g. $PRF_{sbj,d}$ vs $PRF_{sbj,dd}$) in more detail.

2.4.2.2 Assessment of model performance

For a given scan and model, the PRF parameters ($\boldsymbol{G}$ and $\boldsymbol{R}$) were extracted at the first-level as described earlier (Section 2.4.2.1). Subsequently, at the second-level, a 3-fold cross validation approach was implemented using the validation set of the first-level to prevent overfitting. Each scan in the validation set of the first-level CV was partitioned into three segments of about 5 minutes each. One segment was used as the validation set at the second-level for assessing the performance of the model and the remaining two segments were used as the training dataset (at the second-level). This step was repeated three times with each of the three segments used exactly once as the validation data. In each fold, linear regression analysis was performed on the training set to estimate $\boldsymbol{B}$ (5th column of Table 1). Subsequently, the estimated $\boldsymbol{B}$ was used on the validation set (second-level), and the correlation of the model prediction with the GS was calculated. Finally, the mean correlation across the three folds was calculated. For the PRF_{sc} model, one-level cross-validation was used. Specifically, the estimation of both $\boldsymbol{G}$ and $\boldsymbol{B}$ was done on the training set of each fold (i.e., one segment of 5 minutes) and subsequently used on the validation dataset (i.e., the remaining two segments of the same scan).

For each model, the PRF parameters and performance assessment can be obtained from different scan combinations. For instance, in the case of $PRF_{sbj,d}$ for a given subject, the PRF parameters can be estimated from scans R1a (or R1b) and the performance can be assessed on scans R2a (or R2b), yielding 8 total combinations. Therefore, for a given subject, the final performance of a model was assessed for all possible combinations and the average of the obtained values was used at the group level to compare the performance between all examined models (Table 1).

2.4.2.3 Effect of sample size and duration of scan on PRF parameter estimation

To investigate the effect of the number of subjects on parameter estimation in population-specific models (PRF_{ppl} and PRF_{ppl}^{sc}), we repeated the assessment of model performance for the models PRF_{ppl} and PRF_{ppl}^{sc} for the following subject numbers: 1-10, 15, 20, 25, 35 and 40. The subjects were randomly chosen and this part of the analysis was repeated ten times to eliminate biases from "representative" or "non-representative" subjects chosen in a particular iteration. Similarly, to examine the effect of scan duration on the estimation of PRF parameters and investigate the minimum required duration in scan-specific models, we evaluated the performance of the models PRF_{ppl} and PRF_{sc} for scan durations between 1 to 15 minutes in steps of one minute.

2.4.3 Comparison of population-, scan- and voxel-specific PRF curves in individual voxels

Here, we aimed to examine the variability of the PRF curves across voxels. To this end, we compared the performance of a subset of models considered in 2.4.2, particularly the standard models PRF_{stand}, the PRF_{ppl}, PRF_{ppl}^{sc} and PRF_{sc} models, in individual voxels. In addition, we examined the performance of a voxel-specific PRF model, termed PRF_{sc}^{vxl}. PRF_{sc}^{vxl} was simply an extension of PRF_{sc} that allowed variability in the shape of the PRF curve across voxels. For the PRF_{ppl} and PRF_{sc} models, the curves were estimated based on the GS as described in Section 2.4.2. These curves were

subsequently used to extract two physiological regressors that were included in the GLM for a voxel-wise analysis. In a similar manner, the standard models PRF_{stand} were used to extract two physiological regressors for the GLM. The PRF_{sc} model, even though as described earlier is based on Eq. 6 which includes four parameters in $\boldsymbol{B}$, in the voxel-wise analysis it was used as follows: $\boldsymbol{G}$ and $\boldsymbol{B}$ ($\beta_{1,c}, \beta_{2,c}, \beta_{1,r}, \beta_{2,r}$) were estimated based on the GS, and the PRF curves that resulted from these parameters were used to extract two physiological regressors for the GLM. In contrast, for the PRF_{sc}^{vxl} model, the four gamma function corresponding to $\boldsymbol{G}$ and $\boldsymbol{B}$ of PRF_{sc} were used to extract four physiological regressors for the GLM. Similarly, in the case of the PRF_{ppl}^{sc} model, G and B were used to extract four physiological regressors for the GLM. Due to that PRF_{ppl}^{sc} and PRF_{sc}^{vxl} had more physiological regressors in the GLM than the other models examined in this section (4 vs 2), a 3-fold cross validation approach was implemented to assess model performance as described in Section 2.4.2.1.

The comparison of the models was restricted to regions of interest (ROIs) where the models explain significant variance. Specifically, these ROIs were defined as the 5% of voxels in the brain with the highest correlation between the voxel timeseries and the prediction of the corresponding model. The aforementioned five PRF models were examined for CRF and RRF separately as well as both CRF and RRF, yielding 15 models in total. The comparison between the 15 models was repeated on FIX-denoised data using ROIs for each model the ones derived from the original data. Finally, to examine the effect of spatial smoothing on the performance of PRF models, the comparison between the 15 models on the raw data was performed with a FWHM value of 0 mm and 6 mm in addition to the value of 3 mm used for the main analysis.

For visualization purposes, the statistical maps shown here were overlaid on structural images after being transformed to structural space with FSL's FLIRT registration tool (Jenkinson and Smith, 2001) as incorporated in the MANGO software (Lancaster, Martinez; www.ric.uthscsa.edu/mango).

3. Results

3.1 Variability in physiological measurements

The mean HR and BR during resting conditions demonstrated considerable variability across the 164 scans, with the mean HR ranging from 46 to 106 bpm and mean BR from 13 to 23 bpm. To examine the variability across subjects and sessions, all the pairs of scans were grouped in pairs a) from different subjects ($N = 13120$; for a pair of scans the first scan was picked from all 164 scans and the second scan from the 160 scans of the remaining 40 subjects. Thus, the number of unique pairs was 164 x 160 divided by two as the order does not matter), b) from different sessions of the same subject ($N = 41 \cdot 2 \cdot 2 = 164$), and c) from scans of the same session ($N = 41 \cdot 2 = 82$). The differences in HR from the pairs in groups a, b and c yielded standard deviations of 16, 8 and 2 bpm, and the associated variances were found to be different based on an F-test (p-value: $<10^{-49}$). Similarly, the differences in BR from the pairs in groups a, b and c yielded standard deviations of 3.1, 1.7 and 1.0 bpm, and the associated variances were found to be different based on an F-test (p-value: $<10^{-15}$). In Fig. 1, we observe the variability of mean HR and BR across subjects, sessions and scans for 10 representative subjects which clearly illustrates the results from the statistics reported above. For instance, significant differences are found between scans of different subjects such as in the case of subjects S406432 (light blue color) and S555348 (brown color) whereby both four scans of the former subject are characterized by lower mean HR and BR compared to the four scans of the latter one. Also, significant variability is found between sessions within subject such as in the case of subject S203923 (cyan color) whereby both mean HR and BR increase from the first to the second session.

3.2 Variability in the shape of PRF curves across scans

This section, examined the variability in the shape of the PRF_{ppl}, PRF_{ppl}^{sc} and PRF_{sc} curves. In all 164 scans examined in this study, the GS was strongly associated with cardiac and respiratory activity. The first column of Fig. 2 shows the optimal CRF_{ppl} and RRF_{ppl} curves estimated for the 41 subjects using the PRF_{ppl} model that assumes a generalized CRF and RRF for the entire population. Both the PRF_{stand} and PRF_{ppl} curves illustrate a bimodal shape with a positive peak followed by a negative one. However, the amplitude and time of the peaks differ between the curves. The peaks in the CRF_{ppl} appear at much earlier time lags than the ones in the CRF_{stand} reported in Chang et al. (2009) (i.e. 1.2 and 7.0 s for CRF_{ppl}, and 4.1 and 12.4 s for CRF_{stand}). Faster dynamics are also shown in the estimated RRF_{ppl} in comparison with the RRF_{stand} found in Birn et al. (2008b). The positive and negative peaks of the RRF_{ppl} appear at 2.0 and 12.8 s, respectively, whereas the corresponding peaks in the RRF_{stand} are at 3.1 and 15.5 s. Moreover, the estimated PRF_{ppl} curves return to baseline faster than the corresponding PRF_{stand} curves. Last, while the absolute amplitude of

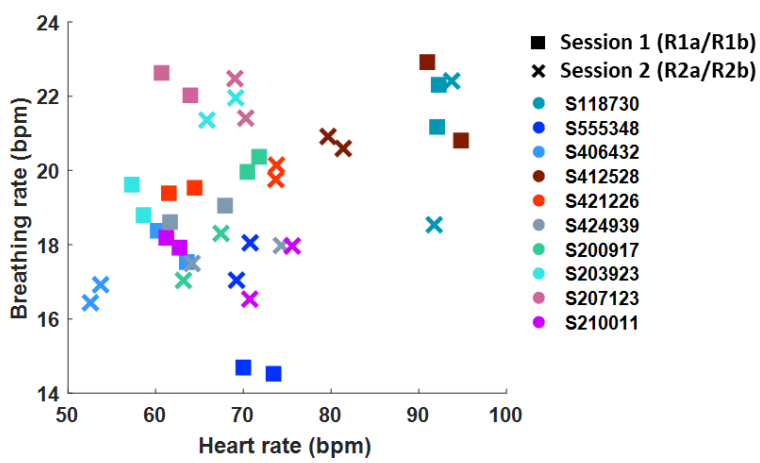

Fig. 1. Scatterplot of mean heart rate (HR) and breathing rate (BR) from scans of 10 representative subjects. Squares and crosses correspond to scans from sessions (days) 1 and 2, respectively, whereas each color indicates a different subject. Both mean HR and BR vary less across scans of the same session than scans across different sessions within subject. In turn, mean HR and BR in the four scans of each subject present less variability than scans from different subjects.

Table 2. Parameters for the $PRF_{ppl}^{(sc)}$ model. The parameters $\boldsymbol{\tau}$ and $\boldsymbol{\delta}$ used in Eq. 5 are an approximate measure for the time of peak and dispersion of the gamma function. The full width at half maximum (FWHM) was calculated numerically.

	$CRF_{ppl}^{(sc)}$		$RRF_{ppl}^{(sc)}$	
	$\boldsymbol{\Gamma_{c_1}(t)}$	$\boldsymbol{\Gamma_{c_2}(t)}$	$\boldsymbol{\Gamma_{r_1}(t)}$	$\boldsymbol{\Gamma_{r_2}(t)}$
Time to peak τ (s)	3.1	5.6	1.9	12.5
Dispersion δ (s)	2.5	0.9	2.9	0.5
FWHM (s)	9.2	8.3	7.0	11.1
Ratio R (β_2/β_1) (only for PRF_{ppl})	N/A	-1.1	N/A	-2.6

the positive and negatives peaks in the PRF_{stand} curves are similar between them, the CRF_{ppl} demonstrate a stronger positive peak and the RRF_{ppl} a stronger negative peak, both of them by a factor of ~2.

The second column of Fig. 2 shows the gamma functions that form the PRF_{ppl} and PRF_{ppl}^{sc} curves while the third column presents scatterplots of $\boldsymbol{B}$ $(\beta_{c_1}, \beta_{c_2}, \beta_{r_1}, \beta_{r_2})$ for all scans that define the shape of the CRF_{ppl}^{sc} and RRF_{ppl}^{sc} curves. Specifically, β_{c_1} (β_{r_1}) and β_{c_2} (β_{r_2}) reflect the direction and magnitude of the first and second peak of the CRF_{ppl}^{sc} (RRF_{ppl}^{sc}) curve, respectively. The parameters of the four gamma functions are listed in Table 2. We observe that all parameters in $\boldsymbol{B}$ for the CRF_{ppl}^{sc} are on the 4th quadrant and are well approximated with a straight line that crosses the origin of the plane corresponding to a ratio R of -1.1. This suggests that the CRF_{ppl}^{sc} curves were fairly consistent across scans and did not significantly deviate from the CRF_{ppl} curve shown in the second column. In contrast, the parameters in $\boldsymbol{B}$ for the RRF_{ppl}^{sc} curves indicate high variability of the curve across scans.

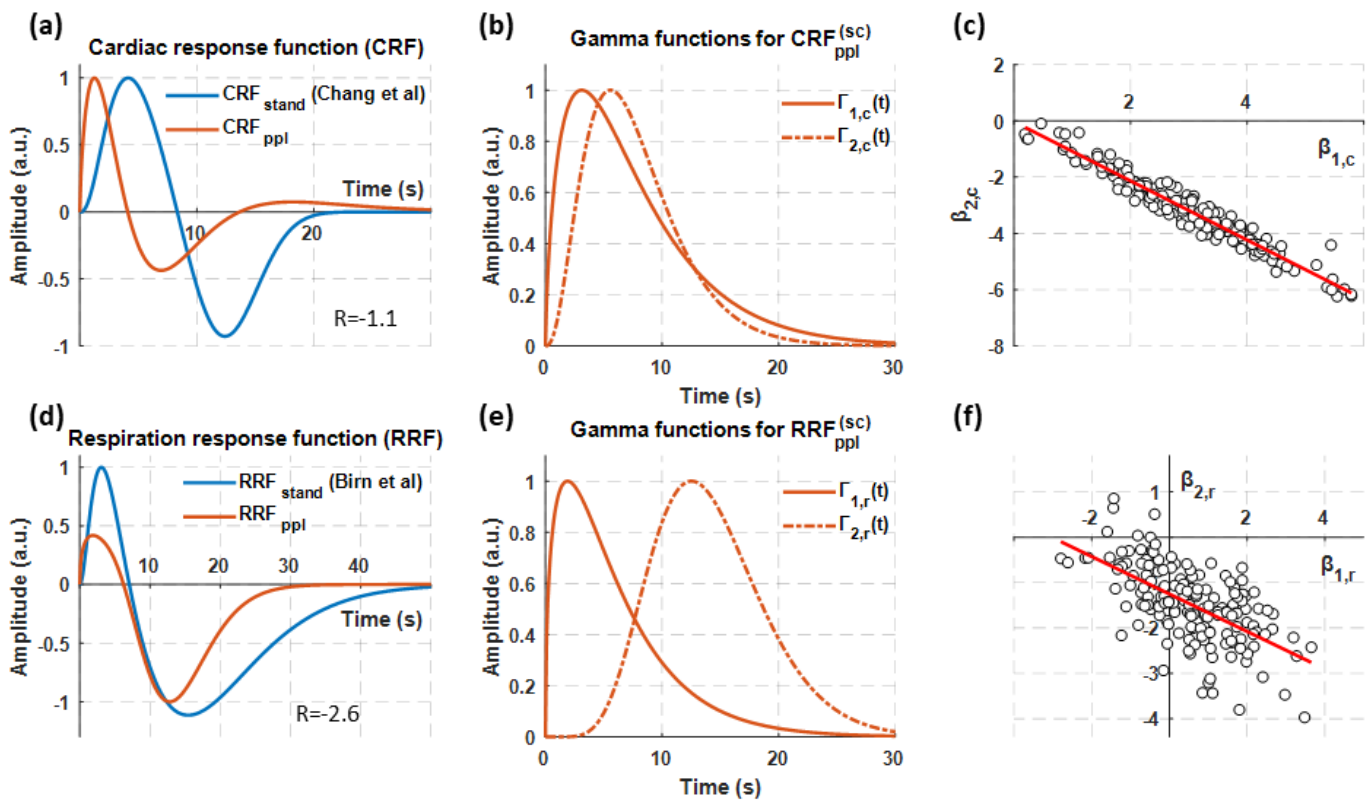

Fig. 2. Estimated gamma functions for the $CRF_{ppl}^{(sc)}$ and $RRF_{ppl}^{(sc)}$ curves. (a) Standard CRF_{stand} and estimated CRF_{ppl} curves. (b) The two gamma functions used to construct the population-specific CRF_{ppl} and CRF_{ppl}^{sc} curves. (c) Scatterplot of parameters in $\boldsymbol{B}$ for the CRF_{ppl}^{sc} model. The circles correspond to the 164 scans and the $\beta_{1,c}$ and $\beta_{2,c}$ parameters reflect the amplitude of the gamma functions $\Gamma_{1,c}$ and $\Gamma_{2,c}$ shown in (b). In a similar manner, (d), (e) and (f) illustrate the results for the models related to RRF.

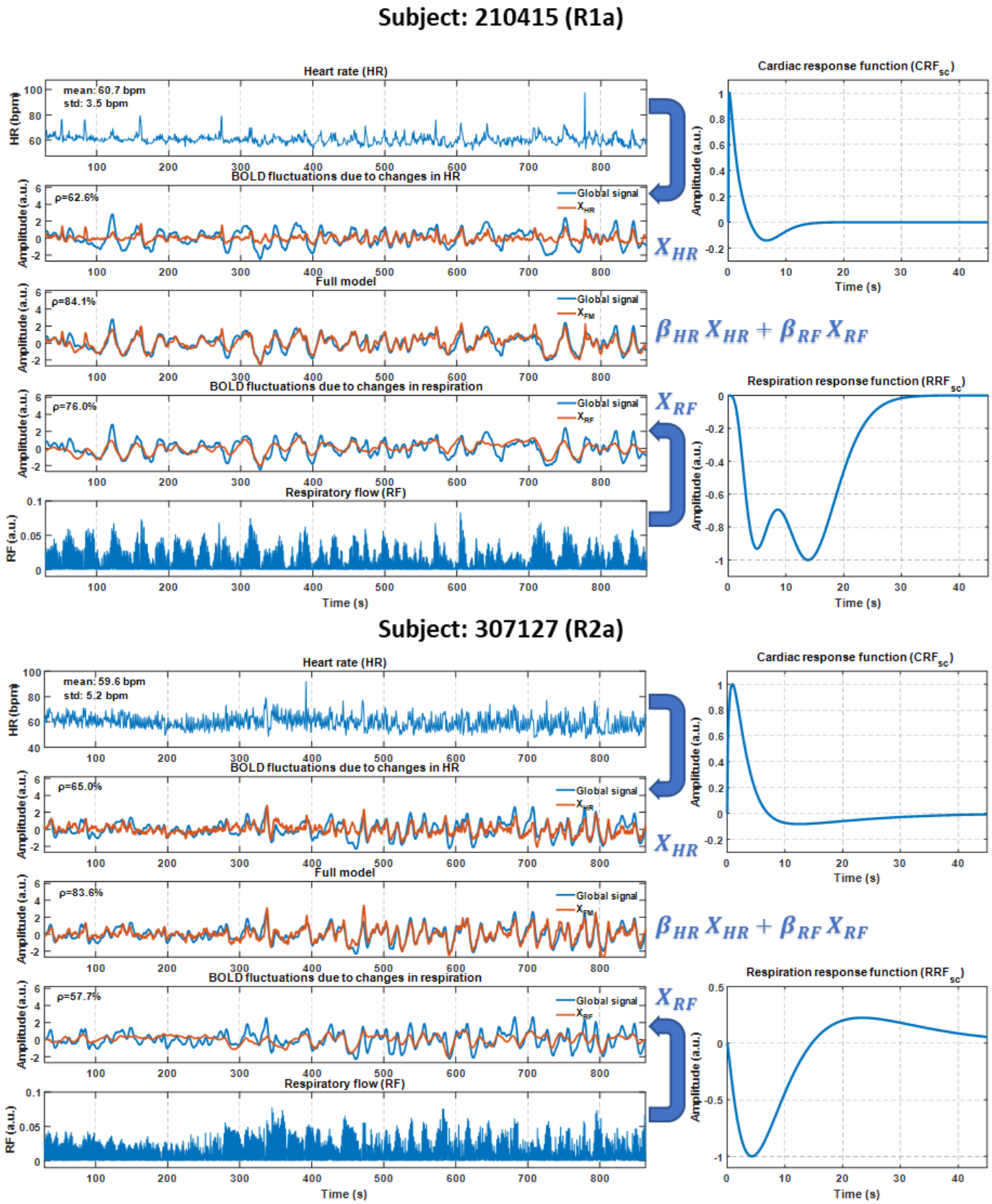

Fig. 3. Demonstration of the PRF_{sc} model for two subjects. First, the HR (1st row of each subject's panel) and respiratory flow (RF; 5th row) were derived from the physiological signals. Subsequently, the PRF parameters that define the scan-specific CRF_{sc} and RRF_{sc} curves were estimated (right column). The physiological regressors X_{HR} and X_{RF} shown in the 2nd and 4th row were modelled as the convolution of HR and RF with the CRF_{sc} and RRF_{sc} curves, respectively. Last, the linear combination of the physiological regressors given by $\boldsymbol{B}$ was used to maximize the explained variance on the GS (3rd row).

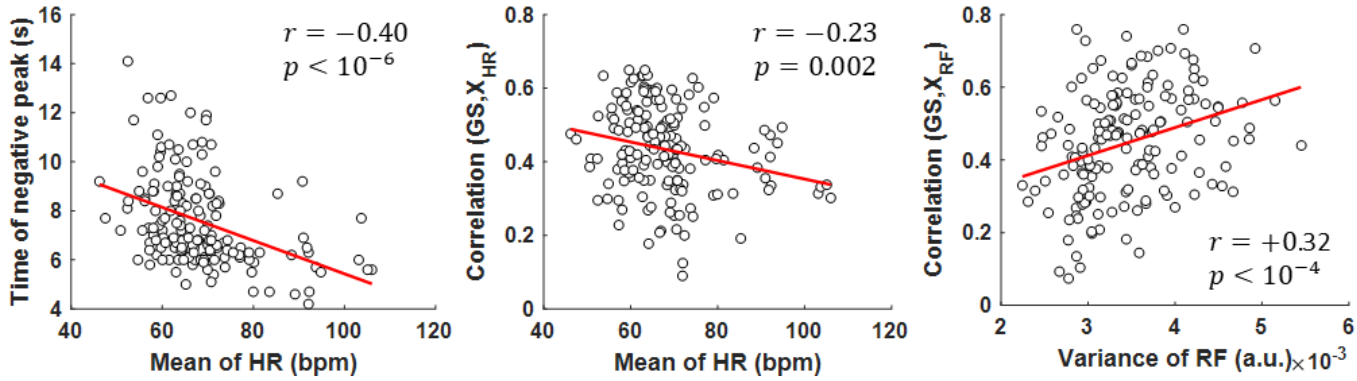

Fig. 4. Scatterplots of physiological variables and features from the PRF_{sc} models. (left) The negative peaks of the CRF_{sc} were negatively correlated with the mean of HR. (middle) The mean HR was anticorrelated with the correlation of the cardiac regressor X_{HR} and GS. (right) The variance of RF was strongly correlated with the correlation of the respiratory regressor and GS.

Fig. 3 illustrates the estimated PRF_{sc} curves for two subjects that demonstrated strong association of the GS with both HR and breathing pattern. Fig. 3 also shows the physiological variables HR and RF as well as the estimated regressors that maximized the correlation with the GS. In this figure, we observe that even though the two subjects had almost the same mean HR, the time evolution of HR of each subject was very different. The HR of subject 210415 was relatively stable with sporadic abrupt increases whereas the HR of subject 30717 had faster fluctuations. With respect to the estimated CRF_{sc} curves, subject 210415 was characterized with a more abrupt increase and faster return to baseline compared to subject 307127. Furthermore, the RF of each subject had a different profile as well while their RRF_{sc} curves differed significantly from the canonical RRF_{stand} and the population-specific RRF_{ppl} curve. The rest of the three scans of subject 210415 exhibited RRF_{sc} curves similar to the RRF_{ppl} (Fig. 2d) while the curves found for the rest of the three scans of subject 307127 were similar to the curve derived from the R2a scan shown in Fig. 3 (supplementary Figs. 4-7).

Of note, the increases in HR for subject 210415 coincided with the increases in RF, and this pattern was found in other subjects as well. However, even though this could raise some concern about the validity of the CRF and RRF curves, it does not seem to affect the results because, as seen in the majority of the subjects, the HR tends to explain faster fluctuations of the GS than the RF. Last, in all four scans of subject 307127, we observed that after the first five minutes the amplitude in both RF and GS increased (Fig. 3 and Supplementary Fig. 4-5). Changes in RF but also in HR accompanied with increases in GS were observed for several subjects after the first few minutes of the scan.

To better understand the properties of the scan-specific PRF_{sc} curves we investigated whether the times of positive and negative peak depend on properties from physiology. Among the different combinations, significant relationship was only found for the CRF_{sc} curves and the subjects' HR. Specifically, we observed that the higher is the mean HR the smallest is the time of negative peak (Fig. 4). Furthermore, we examined whether the fluctuations of HR and breathing pattern have stronger effect on GS under specific physiological states. Fig. 4 shows that the lower was the mean HR the more variance the cardiac regressor explained on the GS whereas the higher was the variance of RF the more variance the respiratory regressor explained on the GS.

3.3 Comparison of population-, subject-, session- and scan-specific PRF curves

The PRF_{ppl} curves, compared to the standard PRF_{stand} curves, demonstrated significant increase of mean correlation from 29.6 % to 51.3 % (Fig. 5; p<0.0001 uncorrected). Extending the PRF_{ppl} model to PRF_{ppl}^{sc} that allows variability in the estimated curve for each scan, the mean correlation significantly increased to 53.2 %. Similarly, optimizing all the parameters for each scan separately (PRF_{sc}) the mean correlation reached 56.1%. While a more flexible model may lead to better fit possibly by overfitting the data, this was not the case here as the models were trained and tested on different datasets. For the PRF_{sc} model that demonstrated the best performance, the contribution of cardiac activity versus respiration was assessed based on paired-sample t-test. While some subjects tended to have more variance due to either cardiac activity or respiration, overall the contribution of both physiological processes was found to be equal.

As illustrated in Fig. 5, $PRF_{sbj,d}$ curves yielded slightly higher mean correlation than PRF_{ppl} curves even though it was not statistically significant. Note that $PRF_{sbj,d}$ models were trained for each subject from a 15-minute scan of the same subject collected in one session and the model performance was assessed on a scan from a different session whereas the PRF_{ppl} models were trained for each subject from the 160 scans of the remaining 40 subjects. Using two scans of 15-minute duration from one session to train the model and validating it with a scan from a different session of the same subject (i.e. $PRF_{sbj,dd}$) the mean correlation was increased even more, but still not significantly higher than for the PRF_{ppl} model. However, a significantly improved fit was achieved when the curves were estimated and validated from different scans collected in the same session (i.e. $PRF_{sbj,s}$). Last, Fig. 5 shows that subject-specific curves performed better when more scans were considered (e.g. $PRF_{sbj,dd}$ yielded better performance than $PRF_{sbj,d}$). Yet, $PRF_{sbj,sdd}$ and $PRF_{sbj,sdd}^{sc}$ models that use the maximum number (3) of within-subject scans for training, did not outperform PRF_{sc} model whereby the parameter estimation and assessment of performance was done on the same scan.

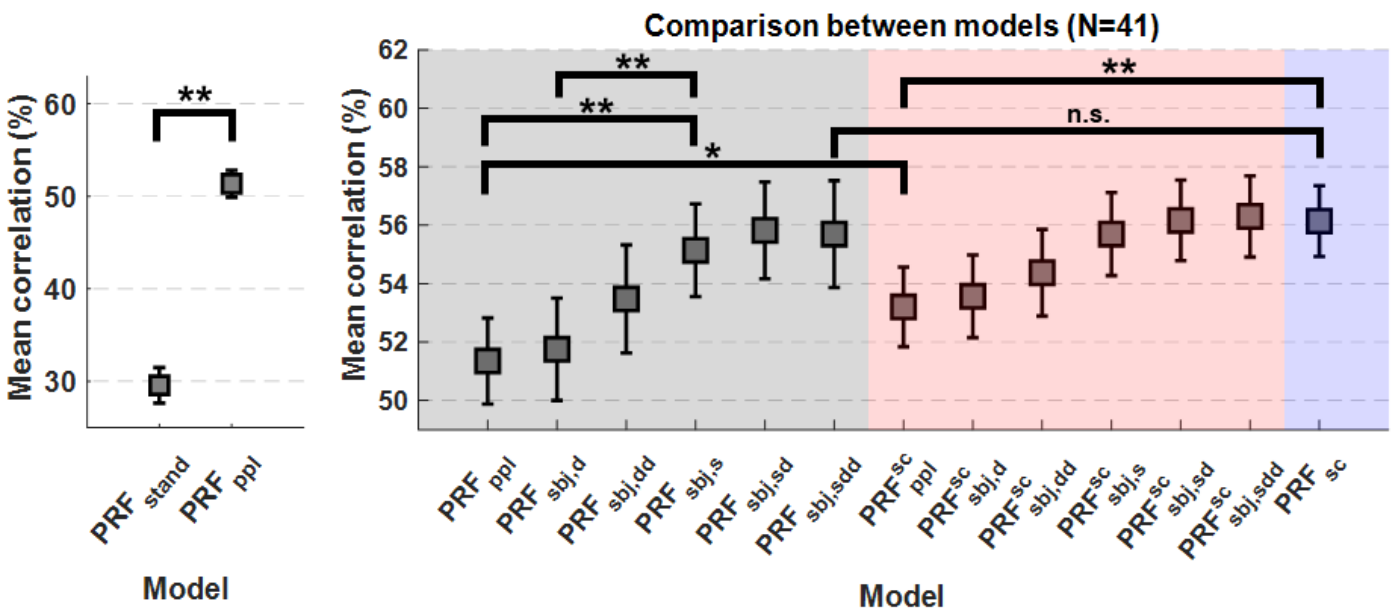

Fig. 5. Correlation of the output of each model with the GS averaged across all subjects. The squares and error bars indicate the mean and standard error of the means of all subjects. The population-specific PRF_{ppl} model yielded significant increase compared to the standard methods (PRF_{stand}). However, models with more flexibility illustrated even higher performance suggesting that the optimal PRF curves varied from subject to subject but also between scans within a subject. *p < 0.01; **P < 0.0001.

3.3.1 *Effect of sample size and duration of scan on PRF parameter estimation*

The performance of the population-specific models, namely the PRF_{ppl} and PRF_{ppl}^{sc} models, depends on how consistent are the curves across subjects as well as how reliable are the estimated parameters. To assess the generalizability of the parameters or whether including data from more subjects could improve the reliability of these models, we repeated the estimation of the model parameters in subsets of subjects. In Fig. 6a, we can see that for the rs-fMRI data of HCP, the performance of the population-specific models increased monotonically from 1 to 10 subjects and reached a plateau at a mean correlation of around 51% and 53 % for the PRF_{ppl} and PRF_{ppl}^{sc} models, respectively. Another important factor that may affect the reliability of a model, particularly in the case of the PRF_{sc} model is the duration of the scan. Fig. 6b shows a comparison of the performance between the least flexible model (PRF_{ppl}) and most flexible model (PRF_{sc}). As we can see, the PRF_{ppl} model started at a relatively higher correlation (44%) for one-minute duration and stabilized at around 51% for scan duration above 5 minutes. While the PRF_{sc} model showed poor performance for duration smaller than 5 minutes, as expected, its performance increased with longer scan durations. Interestingly, it demonstrated the same performance with the PRF_{ppl} model for 5-minute scan duration, which is the minimum scan duration typically used in rs-fMRI studies, and it gradually reached a mean correlation of 56% for 15-minute duration.

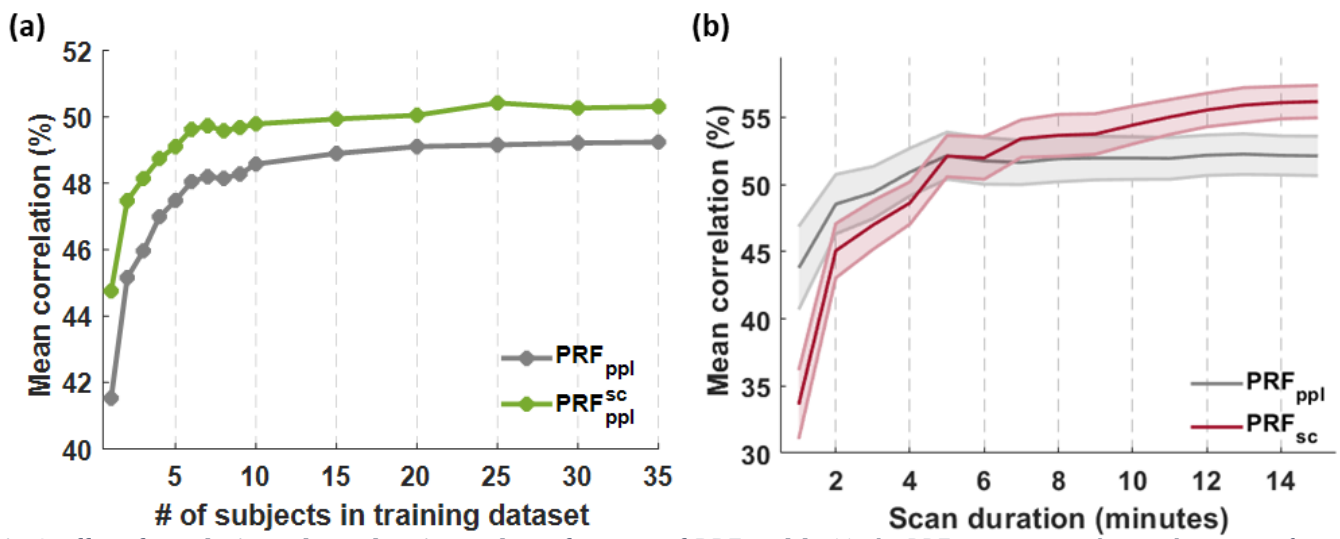

Fig. 6. Effect of sample size and scan duration on the performance of *PRF* models. (a) The *PRF* parameters in the population-specific models, namely PRF_{ppl} and PRF_{ppl}^{sc}, were estimated from subsets of subjects and the performance of the models was assessed on the remaining subjects. Both models reached a plateau at a sample size of around 10 subjects (b) The performance of the least flexible model (i.e. PRF_{ppl}) and the most flexible model (i.e. PRF_{sc}) was assessed on reduced scan durations. Our results suggest that for scan duration longer than 5 minutes the scan-specific PRF_{sc} model explained more variance in GS than the PRF_{ppl} model and a more profound difference was observed as the scan duration increased.

3.4 Model performance in individual voxels

The analysis at the voxel-level yielded similar findings with the analysis based on the fit to GS (Fig. 7). The full PRF_{sc} model (i.e. CRF_{sc} and RRF_{sc}) exhibits the best performance among all models with a mean correlation around 24%. Importantly, the PRF_{sc}^{vxl} model demonstrated slightly lower mean correlation compared to the PRF_{sc} model even though it allows variability in the estimated curves across voxels. In all proposed PRF models, the respiration-related component exhibited higher mean correlation compared to the cardiac-related component, although the difference is not statistically significant ($p > 0.05$). The analysis for assessing model performance at the voxel level was also performed on the resting-state fMRI data that have already been corrected for physiological noise with FIX. The results were similar to the results derived from the raw data, although with overall decreased mean correlation. Once more, the PRF_{sc} model illustrated the best performance with a mean correlation of around 17%.

The brain areas affected by fluctuations in HR and breathing pattern were mainly areas in gray matter and close to blood vessels (Fig. 8). Not surprisingly, the standard methods (PRF_{stand}) and the proposed methods yielded similar maps of areas with physiological noise. However, the explained variance with the proposed methods was significantly higher.

Interestingly, the statistical maps derived in this study demonstrate much finer detail compared to similar maps in other studies (Birn et al., 2008b; Chang et al., 2009; Golestani et al., 2015) which is probably due to the higher spatial resolution (2 mm isotropic voxels) fMRI data acquired in the HCP. However, another factor that affects the resolution in the maps is the spatial smoothing performed during the preprocessing. To better understand its effect, we repeated the analysis and extraction of these maps without spatial smoothing and with a spatial filter that had larger FWHM value (6 mm FWHM instead of 3 mm). As shown in Supplementary Fig. 8-9, the larger were the FWHM value the higher were also the correlation values. However, the 3 mm FWHM that was chosen in this study seems to increase the signal-to-noise (SNR) ratio as assessed from the increased correlation values, without spreading the signal activity, and thus, possibly physiological-related fluctuations, to nearby voxels, with the result of providing finer spatial details in the extracted maps and removing spurious activity.

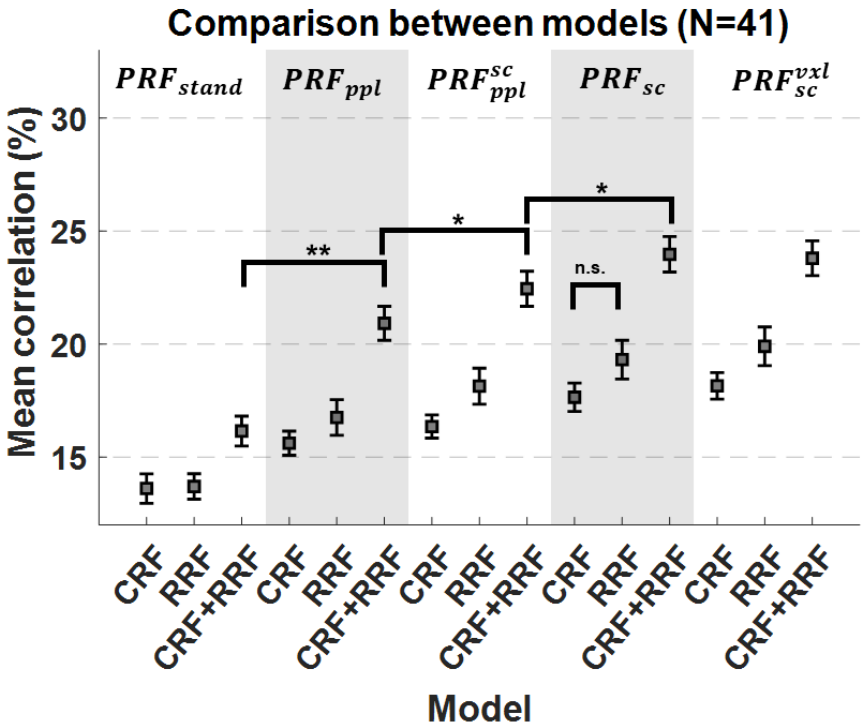

Fig. 7. Correlation of the output of each model with the voxel timeseries in ROIs. The squares and error bars indicate the mean and standard error of the means of all subjects. As with the previous analysis based solely on the GS, the population-specific PRF_{ppl} model yielded significantly increased performance compared to the standard methods (PRF_{stand}). The best performance, however, was achieved with the scan-specific PRF_{sc} model. $*p < 10^{-8}$; $** p < 10^{-13}$.

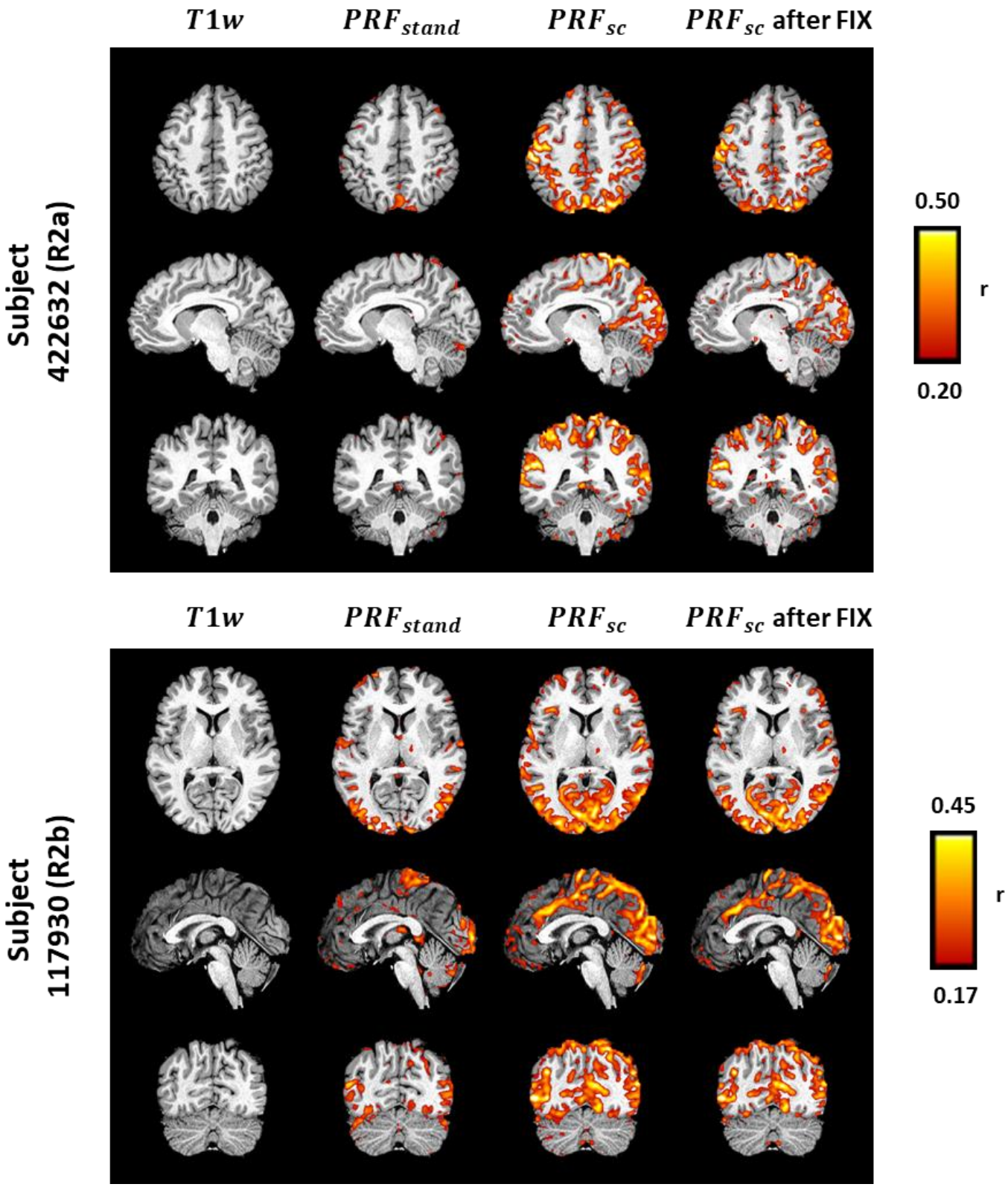

Fig. 8. Maps of the correlation between the physiological models and fMRI timeseries for two representative subjects. (1st column) T_1-weighted images; (2nd & 3rd column) maps derived with the standard (PRF_{stand}) and scan-specific (PRF_{sc}) model, respectively; (4th column) maps derived with the scan-specific model when applied on data previously corrected with FIX. Overall, all models account for substantial variance in gray matter and near large vessels.

The contribution of different sources of physiological noise in fMRI was also examined. The 6 beta parameters for cardiac-related regressors of RETROICOR (3rd order) estimated during the preprocessing were used to construct the pulsatility-driven component of each voxel timeseries which was, subsequently, correlated with each voxel timeseries to extract the correlation map related to pulsatility. The maps related to HR and RF were extracted separately by employing the scan-specific CRF_{sc} and RRF_{sc} models, correspondingly. Fig. 9 shows the contribution of each physiological source for a representative subject on T_2-weighted structural images instead of typical T_1-weighted images as these images demonstrate better contrast than T_1-weighted images for visualizing vessels. We observe that not all areas with large vessels were affected by pulsatility or fluctuations in HR and breathing pattern. Furthermore, both changes in HR and breathing pattern seem to affect areas in gray matter in the cerebrum whereas pulsatility seems to affect areas close to the brainstem. Fig. 10 illustrates the spatial patterns averaged across all subjects for the three aforementioned sources of physiological noise. As in Fig. 9, fluctuations due to changes in HR and RF appear in the same brain areas but in different areas from those affected by cardiac pulsatility. Unfortunately, we could not examine whether the changes in HR and breathing pattern are more likely to induce fluctuations in voxels located at draining veins and sinuses rather than arteries as HCP does not include images for differentiating veins from arteries. However, a visual comparison with voxel-wise probabilistic maps of veins and arteries developed in (Bernier et al., 2018) suggests that indeed voxels nearby large draining vessels are more likely to be affected by changes in HR and breathing pattern, whereas voxels close to arteries are affected by cardiac pulsatility.

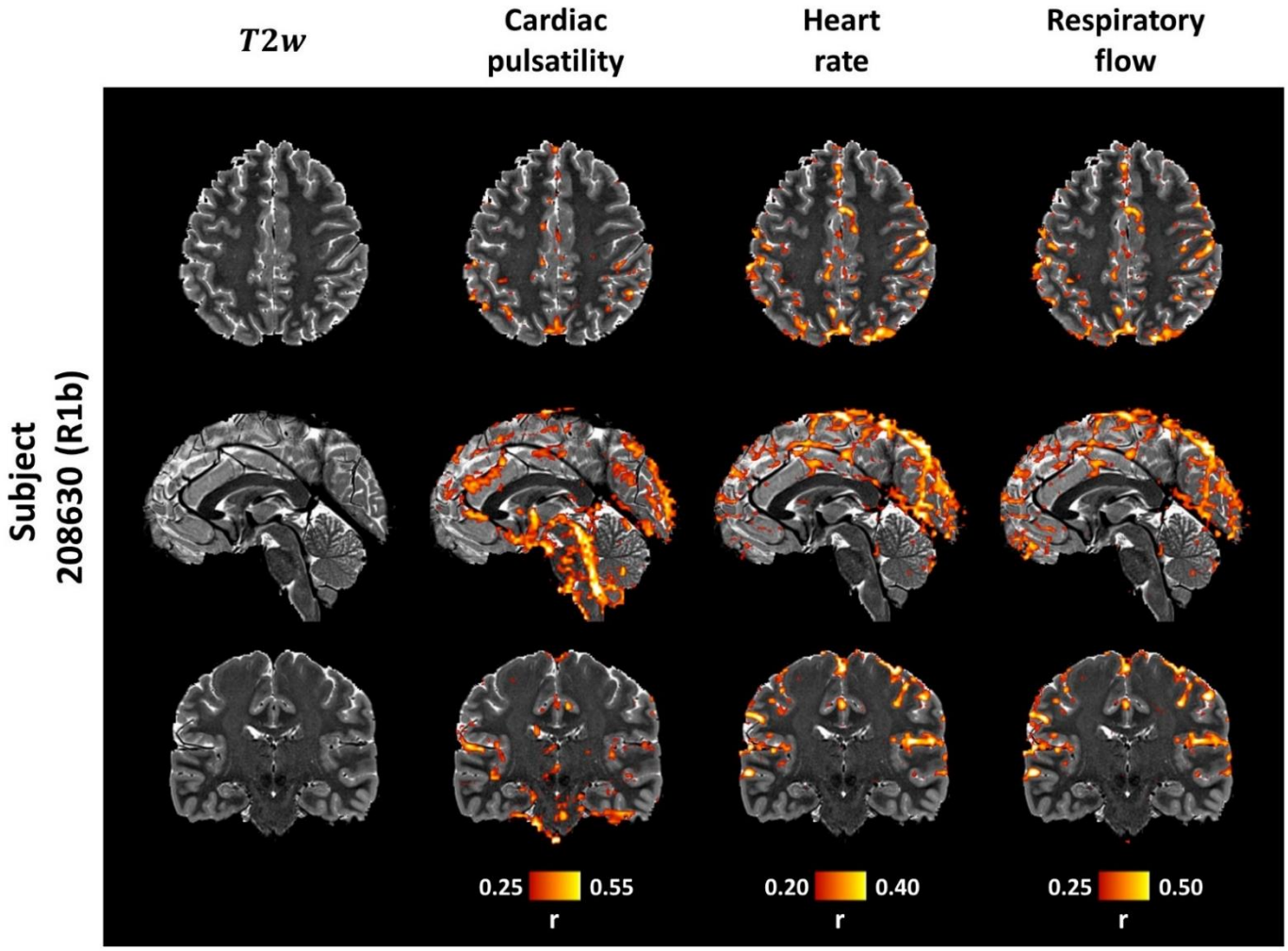

Fig. 9. Contribution of different sources of physiological noise in fMRI for a representative subject. (1st column) T_2-weighted images; (2nd column) maps related to cardiac pulsatility as modelled with RETROICOR; (3rd column) maps related to changes in HR as modelled with the CRF_{sc} model; (4th column) maps related to RF as modelled with the RRF_{sc} model. While the effect of all physiological sources appears in areas close to vessels, the cardiac pulsatility is mainly around the brainstem whereas HR and RF dominate in the occipital and parietal lobes.

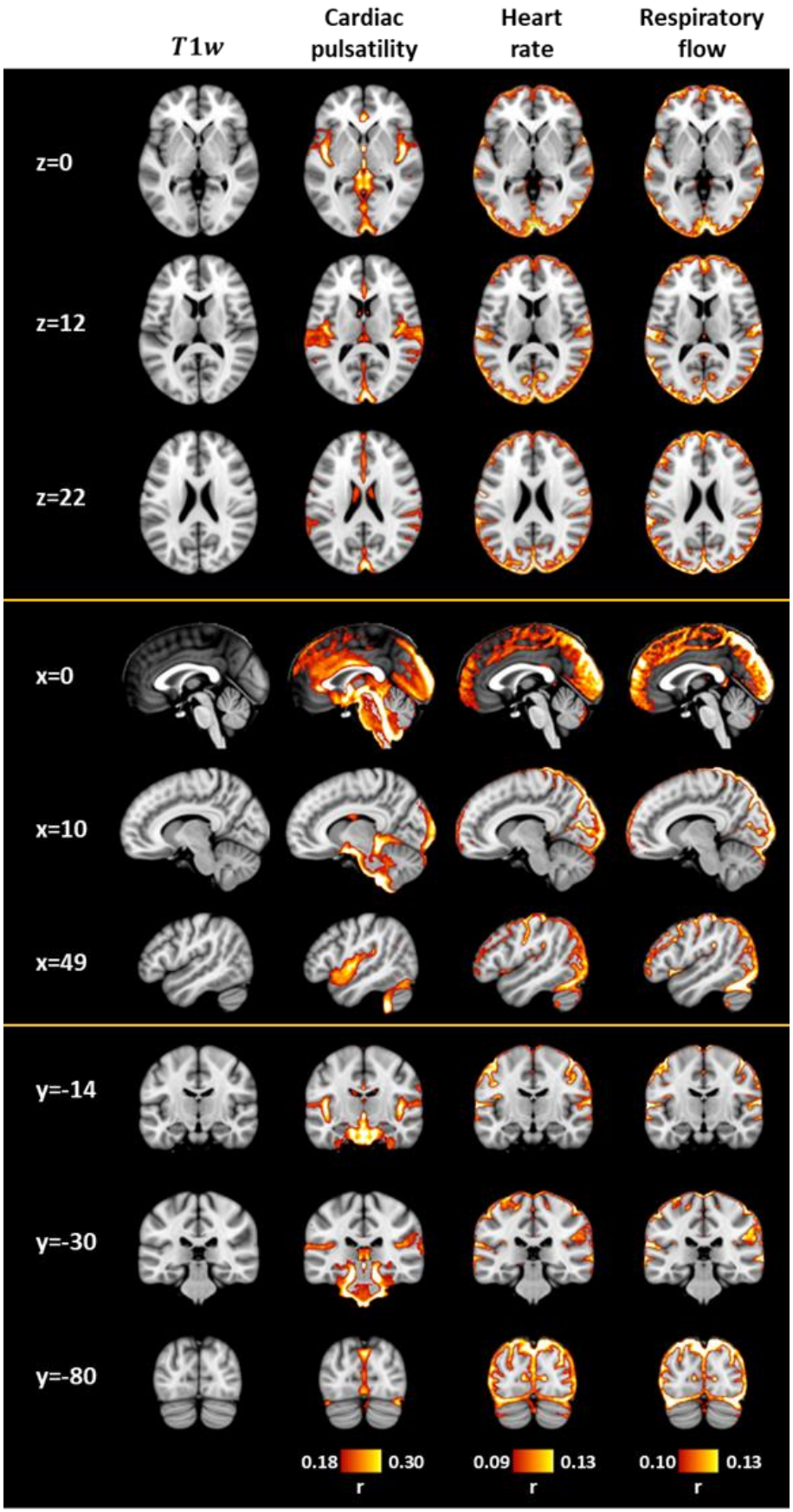

Fig. 10. Contribution of different sources of physiological noise in fMRI averaged across all subjects. (1st column) MNI152 standard-space T_1-weighted average structural template image (1 mm isometric voxel); (2nd column) maps related to cardiac pulsatility as modelled with RETROICOR; (3rd column) maps related to changes in HR as modelled with the CRF_{sc} model; (4th column) maps related to RF as modelled with the RRF_{sc} model. BOLD fluctuations due to cardiac pulsatility appeared close to the basilar and vertebral artery, in the 4th ventricle, in the superior sagittal sinus, in the lateral sulcus and in the medial fissure at the posterior part of the brain and the cingulate gyrus. On the other hand, BOLD fluctuations due to changes in HR and RF were widespread in gray matter mainly in frontal and posterior brain regions as well as in sinuses such as the superior sagittal sinus and the transverse sinuses.

4. Discussion

In this study, we proposed a novel framework for modelling BOLD fluctuations induced by changes in HR and breathing pattern. As suggested in previous studies, linear convolution models were employed where physiological variables are convolved with suitable PRF curves to model the associated physiological-driven BOLD fluctuations. The PRF curves were estimated using numerical optimization techniques that provide several benefits compared to techniques used elsewhere (Birn et al., 2008b; Chang et al., 2009; Falahpour et al., 2013; Golestani et al., 2015). The structure of the curves was defined as the double gamma function which is also the basis of the canonical HRF in SPM and the standard RRF_{stand} (Birn et al., 2008b), and its parameters were restricted in ranges to prevent physiologically implausible. Moreover, in contrast to previous studies, the numerical optimization techniques employed here allow the user to easily impose the properties of a model. For instance, in this work, these techniques allowed the convolution to be done in a pseudo-continuous domain and then downsampled to the fMRI acquisition rate respecting the properties of the hemodynamic processes acquired with fMRI. On a side note, the proposed framework could be applied in other contexts as well such as in HRF estimation.

4.1 Population specific vs standard PRF curves

Using the proposed framework, we derived population specific CRF_{ppl} and RRF_{ppl} curves that explained substantially more variance on the GS and in individual voxel timeseries compared to the standard PRF_{stand} curves (Fig. 5, Fig. **7**). The CRF_{ppl} estimated in this study demonstrated considerably faster dynamics than the one found in Chang et al., (2009). Some of the main differences in the two studies that may explain the results are the following: a) in the previous work the resting-state scan was performed with eyes closed instead of open as done in the HCP, and b) the generalized CRF_{stand} curve was found by estimating first the CRF with the method of maximum likelihood in individual voxels and then averaging across voxels and subjects, whereas, in this study, similar to the approach taken in Falahpour et al. (2013), the CRF estimation was based on the GS of each scan which is strongly driven by physiological noise, and, thus, demonstrates higher SNR. However, we believe that the main reason for the faster dynamics in the CRF_{ppl} curve, is that in previous studies (Chang et al., 2009; Falahpour et al., 2013; Golestani et al., 2015) the HR was averaged in a time window of 4-6 s and then downsampled at a low TR (e.g. 3 s) before further analysis, disregarding the fast fluctuations in HR. Also, due to the sinus arrhythmia commonly observed in young subjects, the smoothed HR may tend to become more similar to the respiratory cycle. As a result, the CRF_{stand} previously reported may capture some of the effects of respiration on the BOLD signal.

Differences were also found between the RRF_{ppl} curve estimated in this study and the standard RRF_{stand} (Birn et al., 2008b), although to a smaller extent. However, in the proposed model, a different feature (RF) was used as an input and, thus, the comparison between RRF_{ppl} and RRF_{stand} curve is not clear. The RF was introduced as a physiological variable derived from the respiratory signal which was preferred rather than RVT as it does not require peak detection, a task not always straightforward with respiratory signals. A possible explanation for the increased performance of the proposed RRF_{ppl} model compared to the standard method is that the RRF_{ppl} curve was estimated on resting-state data with the RF and the GS as the input and output of the model, whereas in Birn et al. (2008b) the RRF_{stand} curve was derived from the BOLD response induced by a deep breath without incorporating the RVT in the estimation stage. Note that Birn et al. (2008b) also reported a poor fit of their method in resting-state fMRI, which was improved only when allowing time-shifting separately for each voxel, an approach that was followed later by others (Bianciardi et al., 2009; Chang and Glover, 2009b). However, time shifting has been shown to inflate the correlation statistics and, therefore, validation of the optimal temporal shift is needed in future studies (Bright et al., 2016).

The population specific CRF_{ppl} curve presented in Fig. 2 is characterized by a peak at 1.2 s and an undershoot at 7.0 s. A possible explanation about the first peak is that increases (decreases) in HR are briefly followed by an increase (decrease) in cardiac output and, in turn, in CBF and BOLD signal. On the other hand, the undershoot may indicate that, several seconds later, the stroke volume decreases (increases) so that the cardiac output returns at its baseline. A positive peak followed by a negative peak was observed for the RRF_{ppl} curve as well. A possible explanation for this behavior

is the following: Increases in RF are followed by increases in the levels of O_2 in cerebral blood which in turn lead to decrease in levels of deoxygenated blood and increase in BOLD signal. However, increases in RF are also followed by decreases in levels of CO_2 in the blood which is a strong vasodilator. As a result, decreases in levels of CO_2 are followed by a decrease in CBF and BOLD signal. The vasoconstriction, however, may be a slower process which can explain the decrease in BOLD signal with a minimum peak at about 13 seconds after the RF increase. In a similar manner, a decrease in RF would lead to an initial decline in BOLD signal followed but a slow overshoot.

4.2 Variability in PRF curves across subjects and scans

Among the different physiological models examined in this study, the scan specific PRF_{sc} model illustrated the best performance. Our results suggest that the PRF_{sc} curves do not only vary across subjects but also across scans of the same subject. Importantly, unless the fMRI scan is shorter than 5 minutes, the PRF_{sc} curves can be robustly derived from the data themselves. As the physiological origin of the CRF and RRF curves is different, their results are discussed separately.

With respect to the CRF, visually inspecting the curves we observed that the scan specific PRF_{sc} curves had slight differences across scans as well as across sessions within subjects. A more systematic comparison revealed that the time of the negative peak of the curve was strongly dependent on the mean HR of the subject, with shorter times linked to higher mean HR. As the mean HR was found to vary significantly between the two sessions within-subject this may explain the differences in CRF_{sc} curves across sessions. Differences in CRF_{sc} curves across sessions within-subject could be attributed also to differences in arterial blood pressure that may vary significantly between scans collected at different days. However, we could not examine this factor as blood pressure measurements were not collected in HCP.

The finding that the negative peak of the curve was strongly dependent on the mean HR of the subject may suggest that the higher is the HR the quicker the stroke volume adjusts to fluctuations in HR in an attempt to maintain the cardiac output stable. In our work, we assumed that the relationship between HR and BOLD signal can be described with a linear time-invariant system. However, it may be the case that a time-variant system whose parameters are expressed as a function of time-varying HR and possibly blood pressure would better explain the fluctuations in GS. Moreover, we observed that the CRF_{sc} explained more variance on the GS for scans with low mean HR. Subsequent analysis showed a strong positive correlation between the mean HR and fluctuations in HR which could indicate that a time-varying CRF is more appropriate for cases where HR varies significantly. On the other hand, a possible explanation that scans with high mean HR did not show strong relationship between fluctuations in HR and GS is that in these scans the subjects were more stressed, which explains the high mean HR, and tended to move more distorting the fMRI data, including the GS, or the subjects were more aroused and in such a mental state that a significant component of the GS fluctuations was neuronal-driven. Nevertheless, despite the slight differences across scans, the majority of the CRF_{sc} curves were more similar to the population specific CRF_{ppl} curve rather than the standard CRF_{stand}.

Regarding the RRF, as mentioned earlier, the population specific RRF_{ppl} curve demonstrated small differences compared to the standard RRF_{stand}. That said, the scan specific RRF_{sc} curves showed a high variability in curves with a large number of scans yielding only negative values in the curve instead of the expected positive peak followed by an undershoot. The differences in the curves could not be attributed to the different patterns in BR or RF. However, the proportion of variance explained on the GS with RF was found to be correlated with the variance of RF. Bear in mind that RF was defined earlier as the square of the derivative of respiratory signal which has a similar form with the framewise displacement measures proposed in the literature for head motion (Power et al., 2012; van Dijk et al., 2012). Head motion is a main source of noise in fMRI as it can cause spin history related motion artifacts in the BOLD signal with finite time memory (Friston et al., 1996). In this context, we could think of RF as an index of relative head motion induced by respiration that is sampled in a higher sampling rate than the motion parameters estimated in fMRI preprocessing during volume realignment. As a result, apart from fluctuations due to changes in CO_2 levels, RF, through convolution with the RRF_{sc}, can potentially remove residuals of motion artifacts that cannot be removed completely with the motion parameters or RETROICOR regressors through linear regression. Moreover, the respiratory-related motion

artifacts may be related to the body type and breathing behavior of each subject as well as the position the subject is placed inside the MRI tube, which could explain the variability of the RRF_{sc} curves across subjects and sessions within-subject and the improved performance of this model compared to a generalized RRF_{ppl} curve, particularly in scans with high variance in RF.

4.3 Physiological noise correction with FIX and GSR

FIX is becoming a very popular tool nowadays for denoising fMRI data as it removes fluctuations due to motion and cardiac pulsatility in an automated manner without the need of physiological recordings (Salimi-Khorshidi et al., 2014). HCP has been using this tool to provide FIX-denoised data and many researchers have been analyzing these data without any further preprocessing (Bijsterbosch et al., 2017; Vidaurre et al., 2017). However, Burgess et al. (2016) have recently demonstrated, using grayordinate plots, that while FIX-denoising substantially reduces spatially specific artifacts it yields only a mild decrease in global fluctuations.

Our study provides further evidence that FIX does not remove global artifacts, and particularly fluctuations due to changes in HR and breathing pattern. These fluctuations are typically found widespread in gray matter and mainly in frontal and posterior brain regions. On a side note, our analysis showed that cardiac pulsatility that is often modelled with RETROICOR is efficiently removed with FIX (results not shown here). It has been suggested that spatial ICA that is used in FIX as well as in other ICA-based denoising techniques such as ICA-AROMA (Pruim et al., 2015b) is mathematically, by design, unable to separate global temporal artifacts from fMRI data (Glasser et al., 2018). However, it is well established that spontaneous fluctuations in physiological processes, that have been shown here and elsewhere to lead to global fluctuations in fMRI (Chang et al., 2009), may lead to invalid results in rs-FC (Birn, 2012; Murphy et al., 2013; Nikolaou et al., 2016) and, therefore, should be taken into consideration in the analysis.

As explained earlier, the GS which is simply the BOLD timeseries averaged across all voxels in the brain, is often regressed out from the fMRI data, in conjunction with other nuisance regressors (Aguirre et al., 1997; Fox et al., 2005) or FIX (Burgess et al., 2016; Siegel et al., 2017), in order to correct for global artifacts. GSR has been shown to improve the correspondence of properties of fMRI rs-FC with observations from neuroanatomy (Fox et al., 2009) and to substantially reduce motion-group differences (Burgess et al., 2016). That said, there is still not consensus in the field whether GSR should be done or not (Liu et al., 2017; Murphy and Fox, 2017). Murphy et al. (2009) first demonstrated that GSR mathematically introduces spurious anticorrelations in rs-FC. Moreover, the next few years, many studies have reported a strong relationship between the fluctuations or amplitude of GS and neuronal-related measures such as electrophysiological activity from intracranial recordings (Scholvinck et al., 2010) and vigilance levels (Chang et al., 2016; Falahpour et al., 2018; Wong et al., 2016, 2013). As a result, in order to facilitate results interpretation, the last few years, reviewers have been encouraging the repetition of rs-FC studies with and without GSR to address whether the results can be attributed to GSR or not, while a recent study has developed a measure dubbed the Impact of the Global Average on Functional Connectivity (IGAFC) that quantifies the extent of the impact of GSR on inferences based on seed-based statistical correlation maps (Carbonell et al., 2014). Furthermore, researchers have started looking for alternatives to GSR. For example, Glasser et al. (2018) have recently proposed the use of temporal ICA after FIX denoising in order to preserve the neuronal-related component of the global signal while removing global structured noise. However, this technique is only applicable to large datasets such as HCP. In addition, Carbonell et al. (2011) have proposed a method based on PCA for regressing out global artifacts and fluctuations that are uncorrelated to network-specific activity even though it cannot ensure the preservation of global neurophysiological activity.

A good alternative to GSR are the PRF models proposed here. These models are trained on a scan-by-scan basis based on the GS and physiological recordings of cardiac activity and respiration. Following the training, the physiological regressors are extracted that can be subsequently removed from the data through linear regression or added in the general linear model as regressors along with regressors of interest. As the physiological regressors are extracted from concurrent physiological recordings, in contrast to GSR and other data-driven techniques, it corrects for physiological-driven fluctuations without any possible loss of neuronal-related fluctuations. The codes for the PRF models presented here are publicly available and can be found on https://github.com/mkassinopoulos/.

5. Conclusion

In this study, we have developed a novel method for removing the effect of fluctuations in HR and breathing pattern in BOLD fMRI data by combining optimization and basis expansion techniques for the robust estimation of subject and scan-specific PRF_{sc} curves. This tool has been tested on data from the Human Connectome Project (HCP) and achieved improved performance compared to current methods, including the standard CRF_{stand} and RRF_{stand}, and FIX.

The proposed framework will be of great importance for researchers interested in studying rs-FC in groups where breathing, heart rhythms or cerebrovascular reactivity can differ. Ultimately, this work can pave the way for understanding the normal and pathological brain as well as accelerate the discovery of connectivity-based biomarkers for diagnosing neurological disorders, as it will contribute towards disentangling the neural vs. physiological sources of rs-FC.

Acknowledgments

This work was supported by the Fonds Recherche Nature et Technologies Quebec (Team Grant awarded to GDM), the Natural Sciences and Engineering Research Council of Canada (Discovery Grant awarded to GDM) and the Canada First Research Excellence Fund (awarded to McGill University for the Healthy Brains for Healthy Lives initiative). MK acknowledges funding from Québec Bio-imaging Network (QBIN).

References

Aguirre, G.K., Zarahn, E., D'Esposito, M., 1997. Empirical Analyses of BOLD fMRI Statistics. Neuroimage 5, 199–212. https://doi.org/10.1006/nimg.1997.0264

Bernier, M., Cunnane, S.C., Whittingstall, K., 2018. The morphology of the human cerebrovascular system. Hum. Brain Mapp. 4962–4975. https://doi.org/10.1002/hbm.24337

Bianciardi, M., Fukunaga, M., van Gelderen, P., Horovitz, S.G., de Zwart, J.A., Shmueli, K., Duyn, J.H., 2009. Sources of functional magnetic resonance imaging signal fluctuations in the human brain at rest: a 7 T study. Magn. Reson. Imaging 27, 1019–1029. https://doi.org/10.1016/j.mri.2009.02.004

Bijsterbosch, J., Harrison, S., Duff, E., Alfaro-Almagro, F., Woolrich, M., Smith, S., 2017. Investigations into within- and between-subject resting-state amplitude variations. Neuroimage 159, 57–69. https://doi.org/10.1016/j.neuroimage.2017.07.014

Birn, R.M., 2012. The role of physiological noise in resting-state functional connectivity. Neuroimage 62, 864–870. https://doi.org/10.1016/j.neuroimage.2012.01.016

Birn, R.M., Diamond, J.B., Smith, M.A., Bandettini, P.A., 2006. Separating respiratory-variation-related fluctuations from neuronal-activity-related fluctuations in fMRI. Neuroimage 31, 1536–48. https://doi.org/10.1016/j.neuroimage.2006.02.048

Birn, R.M., Murphy, K., Bandettini, P.A., 2008a. The effect of respiration variations on independent component analysis results of resting state functional connectivity. Hum. Brain Mapp. https://doi.org/10.1002/hbm.20577

Birn, R.M., Smith, M. a., Jones, T.B., Bandettini, P. a., 2008b. The respiration response function: The temporal dynamics of fMRI signal fluctuations related to changes in respiration. Neuroimage 40, 644–654. https://doi.org/10.1016/j.neuroimage.2007.11.059

Biswal, B., Yetkin, F.Z., Haughton, V.M., Hyde, J.S., 1995. Functional connectivity in the motor cortex of resting human brain using echo-planar MRI. Magn. Reson. Med. 34, 537–541. https://doi.org/10.1002/mrm.1910340409

Bright, M.G., Murphy, K., 2015. Is fMRI “noise” really noise? Resting state nuisance regressors remove variance with network structure. Neuroimage 114, 158–169. https://doi.org/10.1016/j.neuroimage.2015.03.070

Bright, M.G., Tench, C.R., Murphy, K., 2016. Potential pitfalls when denoising resting state fMRI data using nuisance regression. Neuroimage 1–10. https://doi.org/10.1016/j.neuroimage.2016.12.027

Burgess, G.C., Kandala, S., Nolan, D., Laumann, T.O., Power, J.D., Adeyemo, B., Harms, M.P., Petersen, S.E., Barch, D.M., 2016. Evaluation of Denoising Strategies to Address Motion-Correlated Artifacts in Resting-State Functional Magnetic Resonance Imaging Data from the Human Connectome Project. Brain Connect. 6, 669–680. https://doi.org/10.1089/brain.2016.0435

Caballero-Gaudes, C., Reynolds, R.C., 2017. Methods for cleaning the BOLD fMRI signal. Neuroimage 154, 128–149. https://doi.org/10.1016/j.neuroimage.2016.12.018

Carbonell, F., Bellec, P., Shmuel, A., 2014. Quantification of the impact of a confounding variable on functional connectivity confirms anti-correlated networks in the resting-state. Neuroimage 86, 343–353. https://doi.org/10.1016/j.neuroimage.2013.10.013

Carbonell, F., Bellec, P., Shmuel, A., 2011. Global and System-Specific Resting-State fMRI Fluctuations Are Uncorrelated: Principal Component Analysis Reveals Anti-Correlated Networks. Brain Connect. 1, 496–510. https://doi.org/10.1089/brain.2011.0065

Chang, C., Cunningham, J.P., Glover, G.H., 2009. Influence of heart rate on the BOLD signal: The cardiac response function. Neuroimage 44, 857–869. https://doi.org/10.1016/j.neuroimage.2008.09.029

Chang, C., Glover, G.H., 2009a. Effects of model-based physiological noise correction on default mode network anti-correlations and correlations. Neuroimage 47, 1448–1459. https://doi.org/10.1016/j.neuroimage.2009.05.012

Chang, C., Glover, G.H., 2009b. Relationship between respiration, end-tidal CO2, and BOLD signals in resting-state fMRI. Neuroimage 47, 1381–1393. https://doi.org/10.1016/j.neuroimage.2009.04.048

Chang, C., Leopold, D.A., Schölvinck, M.L., Mandelkow, H., Picchioni, D., Liu, X., Ye, F.Q., Turchi, J.N., Duyn, J.H., 2016. Tracking brain arousal fluctuations with fMRI. Proc. Natl. Acad. Sci. 113, 4518–4523. https://doi.org/10.1073/pnas.1520613113

Churchill, N.W., Strother, S.C., 2013. PHYCAA+: An optimized, adaptive procedure for measuring and controlling physiological noise in BOLD fMRI. Neuroimage 82, 306–325. https://doi.org/10.1016/j.neuroimage.2013.05.102

Dagli, M.S., Ingeholm, J.E., Haxby, J. V, 1999. Localization of cardiac-induced signal change in fMRI. Neuroimage 9, 407–415. https://doi.org/10.1006/nimg.1998.0424

Demirtaş, M., Tornador, C., Falcón, C., López-Solà, M., Hernández-Ribas, R., Pujol, J., Menchón, J.M., Ritter, P., Cardoner, N., Soriano-Mas, C., Deco, G., 2016. Dynamic functional connectivity reveals altered variability in functional connectivity among patients with major depressive disorder. Hum. Brain Mapp. 00. https://doi.org/10.1002/hbm.23215

Falahpour, M., Chang, C., Wong, C.W., Liu, T.T., 2018. Template-based prediction of vigilance fluctuations in resting-state fMRI. Neuroimage 174, 317–327. https://doi.org/10.1016/j.neuroimage.2018.03.012

Falahpour, M., Refai, H., Bodurka, J., 2013. Subject specific BOLD fMRI respiratory and cardiac response functions obtained from global signal. Neuroimage 72, 252–264. https://doi.org/10.1016/j.neuroimage.2013.01.050

Fox, M.D., Snyder, A.Z., Vincent, J.L., Corbetta, M., Van Essen, D.C., Raichle, M.E., 2005. The human brain is intrinsically organized into dynamic, anticorrelated functional networks. Proc. Natl. Acad. Sci. U. S. A. 102, 9673–8. https://doi.org/10.1073/pnas.0504136102

Fox, M.D., Zhang, D., Snyder, A.Z., Raichle, M.E., 2009. The global signal and observed anticorrelated resting state brain networks. J. Neurophysiol. 101, 3270–83. https://doi.org/10.1152/jn.90777.2008

Friston, K.J., Williams, S., Howard, R., Frackowiak, R.S., Turner, R., 1996. Movement-related effects in fMRI time-series. Magn. Reson. Med. 35, 346–355. https://doi.org/DOI 10.1002/mrm.1910350312

Glasser, M.F., Coalson, T.S., Bijsterbosch, J.D., Harrison, S.J., Harms, M.P., Anticevic, A., Van Essen, D.C., Smith, S.M., 2018. Using temporal ICA to selectively remove global noise while preserving global signal in functional MRI data. Neuroimage 181, 692–717. https://doi.org/10.1016/j.neuroimage.2018.04.076

Glasser, M.F., Smith, S.M., Marcus, D.S., Andersson, J.L.R., Auerbach, E.J., Behrens, T.E.J., Coalson, T.S., Harms, M.P., Jenkinson, M., Moeller, S., Robinson, E.C., Sotiropoulos, S.N., Xu, J., Yacoub, E., Ugurbil, K., Van Essen, D.C., 2016. The Human Connectome Project's neuroimaging approach. Nat. Neurosci. 19, 1175–87. https://doi.org/10.1038/nn.4361

Glasser, M.F., Sotiropoulos, S.N., Wilson, J.A., Coalson, T.S., Fischl, B., Andersson, J.L., Xu, J., Jbabdi, S., Webster, M., Polimeni, J.R., Van Essen, D.C., Jenkinson, M., 2013. The minimal preprocessing pipelines for the Human Connectome Project. Neuroimage 80, 105–124. https://doi.org/10.1016/j.neuroimage.2013.04.127

Glover, G.H., Li, T.Q., Ress, D., 2000. Image-based method for retrospective correction of physiological motion effects in fMRI: RETROICOR. Magn. Reson. Med. 44, 162–167. https://doi.org/10.1002/1522-2594(200007)44:1<162::AID-MRM23>3.0.CO;2-E

Golestani, A.M., Chang, C., Kwinta, J.B., Khatamian, Y.B., Jean Chen, J., 2015. Mapping the end-tidal CO2 response function in the resting-state BOLD fMRI signal: Spatial specificity, test-retest reliability and effect of fMRI sampling rate. Neuroimage 104, 266–277. https://doi.org/10.1016/j.neuroimage.2014.10.031

Greicius, M.D., Krasnow, B., Reiss, A.L., Menon, V., 2003. Functional connectivity in the resting brain: a network analysis of the default mode hypothesis. Proc Natl Acad Sci U S A 100, 253–258. https://doi.org/10.1073/pnas.0135058100\r0135058100 [pii]

Holland, J.H., 1975. Adaptation in Natural and Artificial Systems. University of Michigan Press, Ann Arbor, MI.

Hu, X., Le, T.H., Parrish, T., Erhard, P., 1995. Retrospective estimation and correction of physiological fluctuation in functional MRI. Magn. Reson. Med. 34, 201–212. https://doi.org/10.1002/mrm.1910340211

Jenkinson, M., Beckmann, C.F., Behrens, T.E.J., Woolrich, M.W., Smith, S.M., 2012. FSL. Neuroimage 62, 782–90. https://doi.org/10.1016/j.neuroimage.2011.09.015

Jenkinson, M., Smith, S., 2001. A global optimisation method for robust affine registration of brain images. Med. Image Anal. 5, 143–156. https://doi.org/10.1016/S1361-8415(01)00036-6

Jones, T.B., Bandettini, P.A., Birn, R.M., 2008. Integration of motion correction and physiological noise regression in fMRI. Neuroimage 42, 582–590. https://doi.org/10.1016/j.neuroimage.2008.05.019

Kasper, L., Bollmann, S., Diaconescu, A.O., Hutton, C., Heinzle, J., Iglesias, S., Hauser, T.U., Sebold, M., Manjaly, Z.M., Pruessmann, K.P., Stephan, K.E., 2017. The PhysIO Toolbox for Modeling Physiological Noise in fMRI Data. J. Neurosci. Methods 276, 56–72. https://doi.org/10.1016/j.jneumeth.2016.10.019

Kay, K.N., Rokem, A., Winawer, J., Dougherty, R.F., Wandell, B.A., 2013. GLMdenoise: A fast, automated technique for denoising task-based fMRI data. Front. Neurosci. 7, 1–15. https://doi.org/10.3389/fnins.2013.00247

Leonardi, N., Richiardi, J., Ville, D. Van De, 2013. Functional Connectivity Eigennetworks Reveal Different Brain Dynamics in Multiple Sclerosis Patients. IEEE Int. Symp. Biomed. Imaging 524–527.

Liang, X., Connelly, A., Calamante, F., 2015. Voxel-wise functional connectomics using arterial spin labeling fMRI: the role of denoising. Brain Connect. 5, 150528105119009. https://doi.org/10.1089/brain.2014.0290

Liu, T.T., Nalci, A., Falahpour, M., 2017. The global signal in fMRI: Nuisance or Information? Neuroimage 150, 213–229. https://doi.org/10.1016/j.neuroimage.2017.02.036

Murphy, K., Birn, R.M., Bandettini, P.A., 2013. Resting-state fMRI confounds and cleanup. Neuroimage 80, 349–359.

https://doi.org/10.1016/j.neuroimage.2013.04.001

Murphy, K., Birn, R.M., Handwerker, D.A., Jones, T.B., Bandettini, P.A., 2009. The impact of global signal regression on resting state correlations: Are anti-correlated networks introduced? Neuroimage 44, 893–905. https://doi.org/10.1016/j.neuroimage.2008.09.036

Murphy, K., Fox, M.D., 2017. Towards a consensus regarding global signal regression for resting state functional connectivity MRI. Neuroimage 154, 169–173. https://doi.org/10.1016/j.neuroimage.2016.11.052

Napadow, V., Dhond, R., Conti, G., Makris, N., Brown, E.N., Barbieri, R., 2008. Brain correlates of autonomic modulation: Combining heart rate variability with fMRI. Neuroimage 42, 169–177. https://doi.org/10.1016/j.neuroimage.2008.04.238

Nikolaou, F., Orphanidou, C., Papakyriakou, P., Murphy, K., Wise, R.G., Mitsis, G.D., 2016. Spontaneous physiological variability modulates dynamic functional connectivity in resting-state functional magnetic resonance imaging. Philos. Trans. A. Math. Phys. Eng. Sci. 374, 20150183-. https://doi.org/10.1098/rsta.2015.0183

Ogawa, S., Lee, T., 1990. Brain magnetic resonance imaging with contrast dependent on blood oxygenation. Proc. … 87, 9868–72. https://doi.org/10.1073/pnas.87.24.9868

Patel, N., Padhiyar, N., 2015. Modified genetic algorithm using Box Complex method: Application to optimal control problems. J. Process Control 26, 35–50. https://doi.org/10.1016/j.jprocont.2015.01.001

Power, J.D., Barnes, K.A., Snyder, A.Z., Schlaggar, B.L., Petersen, S.E., 2012. Spurious but systematic correlations in functional connectivity MRI networks arise from subject motion. Neuroimage 59, 2142–2154. https://doi.org/10.1016/j.neuroimage.2011.10.018

Power, J.D., Plitt, M., Laumann, T.O., Martin, A., 2017. Sources and implications of whole-brain fMRI signals in humans. Neuroimage 146, 609–625. https://doi.org/10.1016/j.neuroimage.2016.09.038

Pruim, R.H.R., Mennes, M., van Rooij, D., Llera, A., Buitelaar, J.K., Beckmann, C.F., 2015a. ICA-AROMA: A robust ICA-based strategy for removing motion artifacts from fMRI data. Neuroimage 112, 267–277. https://doi.org/10.1016/j.neuroimage.2015.02.064

Pruim, R.H.R., Mennes, M., van Rooij, D., Llera, A., Buitelaar, J.K., Beckmann, C.F., 2015b. ICA-AROMA: A robust ICA-based strategy for removing motion artifacts from fMRI data. Neuroimage 112, 267–277. https://doi.org/10.1016/j.neuroimage.2015.02.064

Qing, Z., Dong, Z., Li, S., Zang, Y., Liu, D., 2015. Global signal regression has complex effects on regional homogeneity of resting state fMRI signal. Magn. Reson. Imaging 33, 1306–1313. https://doi.org/10.1016/j.mri.2015.07.011

Salimi-Khorshidi, G., Douaud, G., Beckmann, C.F., Glasser, M.F., Griffanti, L., Smith, S.M., 2014. Automatic denoising of functional MRI data: Combining independent component analysis and hierarchical fusion of classifiers. Neuroimage 90, 449–468. https://doi.org/10.1016/j.neuroimage.2013.11.046

Scholvinck, M.L., Maier, A., Ye, F.Q., Duyn, J.H., Leopold, D.A., 2010. Neural basis of global resting-state fMRI activity. Proc. Natl. Acad. Sci. 107, 10238–10243. https://doi.org/10.1073/pnas.0913110107

Sheline, Y.I., Price, J.L., Yan, Z., Mintun, M.A., 2010. Resting-state functional MRI in depression unmasks increased connectivity between networks via the dorsal nexus. Proc. Natl. Acad. Sci. 107, 11020–11025. https://doi.org/10.1073/pnas.1000446107

Shmueli, K., van Gelderen, P., de Zwart, J. a., Horovitz, S.G., Fukunaga, M., Jansma, J.M., Duyn, J.H., 2007. Low-frequency fluctuations in the cardiac rate as a source of variance in the resting-state fMRI BOLD signal. Neuroimage 38, 306–320. https://doi.org/10.1016/j.neuroimage.2007.07.037

Siegel, J.S., Mitra, A., Laumann, T.O., Seitzman, B.A., Raichle, M., Corbetta, M., Snyder, A.Z., 2017. Data quality influences observed links between functional connectivity and behavior. Cereb. Cortex 27, 4492–4502. https://doi.org/10.1093/cercor/bhw253

Smith, S.M., Fox, P.T., Miller, K.L., Glahn, D.C., Fox, P.M., Mackay, C.E., Filippini, N., Watkins, K.E., Toro, R., Laird, A.R., Beckmann, C.F., 2009. Correspondence of the brain's functional architecture during activation and rest. Proc. Natl. Acad. Sci. U. S. A. 106, 13040–5. https://doi.org/10.1073/pnas.0905267106

van den Heuvel, M.P., Hulshoff Pol, H.E., 2010. Exploring the brain network: A review on resting-state fMRI functional connectivity. Eur. Neuropsychopharmacol. 20, 519–534. https://doi.org/10.1016/j.euroneuro.2010.03.008

van Dijk, K.R.A., Sabuncu, M.R., Buckner, R.L., 2012. The influence of head motion on intrinsic functional connectivity MRI. Neuroimage 59, 431–438. https://doi.org/10.1016/j.neuroimage.2011.07.044

Van Essen, D.C., Smith, S.M., Barch, D.M., Behrens, T.E.J., Yacoub, E., Ugurbil, K., 2013. The WU-Minn Human Connectome Project: An overview. Neuroimage 80, 62–79. https://doi.org/10.1016/j.neuroimage.2013.05.041

Vidaurre, D., Smith, S.M., Woolrich, M.W., 2017. Brain network dynamics are hierarchically organized in time. Proc. Natl. Acad. Sci. 201705120. https://doi.org/10.1073/pnas.1705120114

Wise, R.G., Ide, K., Poulin, M.J., Tracey, I., 2004. Resting fluctuations in arterial carbon dioxide induce significant low frequency variations in BOLD signal. Neuroimage 21, 1652–1664. https://doi.org/10.1016/j.neuroimage.2003.11.025

Wong, C.W., DeYoung, P.N., Liu, T.T., 2016. Differences in the resting-state fMRI global signal amplitude between the eyes open and eyes closed states are related to changes in EEG vigilance. Neuroimage 124, 24–31. https://doi.org/10.1016/j.neuroimage.2015.08.053

Wong, C.W., Olafsson, V., Tal, O., Liu, T.T., 2013. The amplitude of the resting-state fMRI global signal is related to EEG vigilance measures. Neuroimage 83, 983–990. https://doi.org/10.1016/j.neuroimage.2013.07.057

Woodward, N.D., Cascio, C.J., 2015. Resting-State Functional Connectivity in Psychiatric Disorders. JAMA psychiatry 72, 743–744. https://doi.org/10.1001/jamapsychiatry.2015.0101.2